

Transverse Single-Spin Asymmetry for Diffractive  
Electromagnetic Jets with  $p^\uparrow + p$  Collisions at  
 $\sqrt{s} = 200$  GeV

Xilin Liang

February 14, 2025

# Contents

<b>1</b>	<b>Introduction</b>	<b>8</b>
<b>2</b>	<b>Dataset and Quality Assurance (QA)</b>	<b>10</b>
2.1	General information for the dataset . . . . .	10
2.2	Triggers . . . . .	10
2.3	Calibration . . . . .	11
<b>3</b>	<b>Single Diffractive Process and Event Selection</b>	<b>14</b>
3.1	Electromagnetic jet reconstruction and cuts . . . . .	15
3.2	Event property cut . . . . .	16
3.3	BBC East veto cut . . . . .	19
3.4	Roman Pot track cut . . . . .	19
<b>4</b>	<b>Corrections</b>	<b>23</b>
4.1	Underlying Event (UE) correction . . . . .	23
4.2	Detector level to particle level EM-jet energy correction . . . . .	23
<b>5</b>	<b>Rapidity Gap (RG) events study</b>	<b>26</b>
5.1	Motivation . . . . .	26
5.2	Event selection for RG events . . . . .	26
5.3	Fraction of single diffractive events in rapidity gap events . . . . .	27
<b>6</b>	<b>Semi-exclusive process study</b>	<b>29</b>
6.1	West BBC veto cuts . . . . .	30
6.2	Roman Pot (RP) track cut . . . . .	31
6.3	Energy sum cuts . . . . .	33
<b>7</b>	<b>Background study</b>	<b>37</b>
7.1	Zerobias event study . . . . .	37
7.2	Mix event background for energy sum cut study . . . . .	38

<b>8</b>	<b>Systematic Uncertainty for <math>A_N</math></b>	<b>41</b>
8.1	Method for systematic uncertainty . . . . .	41
8.2	Systematic uncertainty for the BBC veto cuts . . . . .	42
8.3	Ring of Fire . . . . .	42
8.4	Energy sum cut uncertainty . . . . .	42
8.5	Polarization uncertainty . . . . .	43
8.6	Summary for the systematic uncertainty . . . . .	44
<b>9</b>	<b><math>A_N</math> Analysis Method and Results</b>	<b>49</b>
9.1	$A_N$ Extraction . . . . .	49
9.2	Single diffractive EM-jet $A_N$ . . . . .	50
9.3	Rapidity gap events EM-jet $A_N$ . . . . .	52
9.4	Semi-exclusive EM-jet $A_N$ . . . . .	52
<b>10</b>	<b>Cross section fraction study</b>	<b>56</b>
<b>11</b>	<b>Conclusion</b>	<b>59</b>
<b>A</b>	<b>Run list</b>	<b>60</b>
<b>B</b>	<b>Derivation for the AC events effect to the uncertainty</b>	<b>64</b>
<b>C</b>	<b>Cross-ratio fit quality results</b>	<b>66</b>

# List of Figures

2.1	Example of EM-jet distribution at FMS before additional hot channel masking. The red color area in this plot indicates the possible hot channels. . . . .	12
2.2	Example of EM-jet distribution at FMS after additional hot channel masking. . . . .	13
3.1	Diagram for single diffractive process. . . . .	14
3.2	EM-jet transverse momentum ( $p_T$ ) vs energy (E) before correction. . . . .	17
3.3	Number of EM-jets in the event. . . . .	18
3.4	East RP $\theta_X$ and $\theta_Y$ distributions for 7 different East RP track $\xi$ ranges with only applying East BBC ADC sum $< 150$ . . . . .	19
3.5	The small (left) and large (right) East BBC ADC sum distribution after the rough East RP $\theta_X$ and $\theta_Y$ cuts . . . . .	20
3.6	East RP $\theta_X$ and $\theta_Y$ distributions for three East RP track $\xi$ ranges. . . . .	21
3.7	East RP track $p_X$ and $p_Y$ distributions for three East RP track $\xi$ ranges. The black curves indicate the ranges of accepted East RP track $p_X$ and $p_Y$ cuts. . . . .	22
4.1	UE distribution for diffractive EM-jet analysis. The left plot shows the subtraction term $\rho \times A$ . The right plot shows the EM-jet energy distribution after the UE correction. . . . .	24
4.2	EM-jet energy distribution in particle level (y-axis) and detector level (x-axis) from the FMS simulation. . . . .	25
4.3	The profile of the EM-jet energy distribution with particle level and detector level. The black points are the correlation between the EM-jet energy at the particle level and detector level. The red curves are the fit for the black points. . . . .	25
5.1	Diagram for rapidity gap events. . . . .	27
6.1	Diagram for semi-exclusive process. . . . .	29

6.2	West RP $\theta_X$ and $\theta_Y$ distributions for 9 different East RP track $\xi$ ranges with only applying West BBC ADC sum $< 150$ . . . . .	32
6.3	Small BBC west ADC sum distribution after the rough west RP cuts. . . . .	32
6.4	Large BBC west ADC sum distribution after the rough west RP cuts. . . . .	33
6.5	West RP $\theta_X$ and $\theta_Y$ distributions for 9 different East RP track $\xi$ ranges after applying West BBC veto cuts. . . . .	34
6.6	West RP track $p_X$ and $p_Y$ distributions for nine West RP track $\xi$ ranges. The black curves indicate the ranges of accepted West RP track $p_X$ and $p_Y$ cuts. . . . .	35
6.7	Energy sum cuts for 5 different EM-jet $x_F$ regions . . . . .	36
7.1	Example for mix event energy sum background study for EM-jet with $0.2 < x_F < 0.25$ . . . . .	39
7.2	Mix event energy sum background study results for each EM-jet $x_F$ regions. In each plot, the red curve indicates the energy sum distribution in data, while the black curve indicates the scaled mix event energy sum background. . . . .	40
9.1	Example of the raw asymmetry (raw $A_N$ ) extraction with the cosine fit. This is the fit for calculating the raw asymmetry for single diffractive EM-jet $A_N$ with all photon multiplicity at the EM-jet $0.25 < x_F < 0.3$ . . . . .	50
9.2	$A_N$ for single diffractive events as a function of $x_F$ for three different photon multiplicity cases: all photon multiplicity (top), one or two-photon multiplicity (middle), and three or more photon multiplicity (bottom). The $A_N$ for $x_F < 0$ (red points) shifts -0.013 along the x-axis. . . . .	51
9.3	$A_N$ for rapidity gap events as a function of $x_F$ for three different photon multiplicity cases: all photon multiplicity (top), one or two-photon multiplicity (middle), and three or more photon multiplicity (bottom). The $A_N$ for $x_F < 0$ (red points) shifts -0.013 along the x-axis. . . . .	53
9.4	$A_N$ for inclusive process (red), single diffractive process (blue), and the rapidity gap events (purple) as a function of $x_F$ for one or two-photon multiplicity case (top panel) and three or more-photon multiplicity (bottom panel). The $A_N$ for single diffractive process shifts -0.008 along the x-axis, and the $A_N$ for rapidity gap events shifts +0.008 along the x-axis . . . . .	54

9.5	$A_N$ for the semi-exclusive process with 1 or 2 photon multiplicity EM-jets as a function of EM-jet $x_F$ . The blue points are for $x_F > 0$ , while the red points are for $x_F < 0$ . . . . .	55
10.1	Cross section fraction of the single diffractive process ( $\sigma_{SD}$ ) to the inclusive process ( $\sigma_{inc}$ ) as a function of $x_F$ . . . . .	58
C.1	$\chi^2$ for the fit for all the data points for all three processes. . . . .	67
C.2	Distribution of the constant term from the fit divided by its uncertainty . . . . .	67

# List of Tables

2.1	Trigger name lists and trigger ID for run 15 . . . . .	11
3.1	EM-jet trigger threshold $p_T$ cut, listed by trigger name and trigger ID. . . . .	17
3.2	4 acceptable 4-bit spin patterns . . . . .	18
3.3	Rough cuts for East RP track $\theta_X$ by different East RP track $\xi$ . . . . .	20
3.4	Final cuts for East RP track $\theta_X$ by three $\xi$ regions . . . . .	21
3.5	East RP track $p_X$ and $p_Y$ final cuts . . . . .	22
4.1	Parameters for the 6th-order polynomial . . . . .	25
6.1	Rough west RP $\theta_X$ cuts . . . . .	31
6.2	Final west RP $\theta_X$ cuts . . . . .	34
6.3	Final west RP $p_X$ and $p_Y$ cuts . . . . .	35
6.4	Energy sum cuts for semi-exclusive process . . . . .	36
7.1	Signal region and background region for energy sum spectrum in data . . . . .	39
7.2	Fraction of the mix event energy sum background for each EM-jet $x_F$ region . . . . .	40
8.1	List of BBC veto cut values for systematic uncertainty study. . . . .	42
8.2	Energy sum cuts for semi-exclusive process in the energy sum cut uncertainty study . . . . .	43
8.3	Systematic uncertainty for blue beam $A_N$ for all photon multiplicity EM-jets from single diffractive process . . . . .	45
8.4	Systematic uncertainty for yellow beam $A_N$ for all photon multiplicity EM-jets from single diffractive process . . . . .	45
8.5	Systematic uncertainty for blue beam $A_N$ for 1 or 2 photon multiplicity EM-jets from single diffractive process . . . . .	45
8.6	Systematic uncertainty for yellow beam $A_N$ for 1 or 2 photon multiplicity EM-jets from single diffractive process . . . . .	46

8.7	Systematic uncertainty for blue beam $A_N$ for 3 or more photon multiplicity EM-jets from single diffractive process . . . . .	46
8.8	Systematic uncertainty for yellow beam $A_N$ for 3 or more photon multiplicity EM-jets from single diffractive process . . . . .	46
8.9	Systematic uncertainty for blue beam $A_N$ for all photon multiplicity EM-jets from rapidity gap events . . . . .	46
8.10	Systematic uncertainty for yellow beam $A_N$ for all photon multiplicity EM-jets from rapidity gap events . . . . .	46
8.11	Systematic uncertainty for blue beam $A_N$ for 1 or 2 photon multiplicity EM-jets from rapidity gap events . . . . .	47
8.12	Systematic uncertainty for yellow beam $A_N$ for 1 or 2 photon multiplicity EM-jets from rapidity gap events . . . . .	47
8.13	Systematic uncertainty for blue beam $A_N$ for 3 or more photon multiplicity EM-jets from rapidity gap events . . . . .	47
8.14	Systematic uncertainty for yellow beam $A_N$ for 3 or more photon multiplicity EM-jets from rapidity gap events . . . . .	47
8.15	Systematic uncertainty for blue beam $A_N$ for 1 or 2 photon multiplicity EM-jets from semi-exclusive process . . . . .	48
8.16	Systematic uncertainty for yellow beam $A_N$ for 1 or 2 photon multiplicity EM-jets from semi-exclusive process . . . . .	48
A.1	Run list . . . . .	60



# 1 Chapter 1

## 2 Introduction

3 Transverse single-spin asymmetries ( $A_N$ ), which are defined as left-right asym-  
4 metries of the particle production with respect to the plane defined by the  
5 momentum and spin directions of the polarized beam, have been observed to be  
6 large for charged- and neutral-hadron production in hadron-hadron collisions  
7 over a couple of decades [1, 2, 3, 4, 5]. In pQCD, however, the  $A_N$  is predicted  
8 to be small and close to zero in high energy collisions [6]. There are two major  
9 frameworks that can provide a potential explanation for such sizeable asymme-  
10 tries. The first one is the transverse-momentum-dependent (TMD) contribu-  
11 tions from the initial-state quark and gluon Sivers functions and/or the final-  
12 state Collins fragmentation functions. In the Sivers mechanism, the asymmetry  
13 comes from the correlation between the proton spin and the parton transverse  
14 momentum [7], while the Collins effect arises from the correlation between the  
15 spin of the fragmenting quark and the outgoing hadron's transverse momentum  
16 [8]. Another framework is based on the twist-3 contributions in the collinear  
17 factorization framework, including the quark-gluon or gluon-gluon correlations  
18 and fragmentation functions [9].

19 According to the study by CMS Collaboration [10], diffractive interactions  
20 contribute to about a significant fraction ( $\sim 25\%$ ) of the total inelastic p+p  
21 cross section at high energies. The simulation for hard diffractive events based  
22 on PYTHIA-8 predicts that the fraction of diffractive cross section in the total  
23 inclusive cross section at the forward region is about 20% [4]. In recent years,  
24 analyses of  $A_N$  for forward  $\pi^0$  and electromagnetic jets (EM-jets) in  $p^\uparrow + p$   
25 collisions at STAR indicated that there might be non-trivial contributions to  
26 the large  $A_N$  from diffractive processes [5, 11]. Measuring the  $A_N$  of diffractive  
27 process will provide an opportunity to study the properties and understand the  
28 diffractive exchange in p+p collisions.

29 In this study, we will explore the  $A_N$  for the events with unpolarized proton

<sup>30</sup> intact (single diffractive process) and the events with polarized proton intact  
<sup>31</sup> (the semi-exclusive process).

## 32 Chapter 2

# 33 Dataset and Quality 34 Assurance (QA)

### 35 2.1 General information for the dataset

36 The single diffractive and the semi-exclusive EM-jet  $A_N$  analyses utilize polar-  
37 ized p+p collision at  $\sqrt{s} = 200$  GeV taken in run 15. Details of the data set are  
38 listed as follow:

- 39 • Trigger setup name: production\_pp200trans\_2015
- 40 • Data stream: fms
- 41 • Production tag: P15ik
- 42 • File type: MuDst files in Distributed Disk (DD)

43 The analysis generates smaller size data stream files (NanoDst) from the  
44 MuDst files, applying trigger filter (described in Sec. (2.2)) and jet reconstruc-  
45 tion (described in Sec. 3.1). In addition, the events with at least one Roman  
46 Pot track are required for diffractive EM-jet  $A_N$  analysis when generating the  
47 DST files.

### 48 2.2 Triggers

49 9 triggers for FMS are used for this analysis. The triggers with their ID are  
50 listed in Table (2.1). However, the FMS-sm-bs3 trigger is also considered a  
51 source of background. Therefore, the effect of this trigger will be studied as  
52 systematic uncertainty, which will be explained in 8.3.

Table 2.1: Trigger name lists and trigger ID for run 15

Trigger name	Trigger ID
FMS-JP0	480810 / 480830
FMS-JP1	480809 / 480829
FMS-JP2	480808 / 480828
FMS-sm-bs1	480801 / 480821 / 480841
FMS-sm-bs2	480802 / 480822
FMS-sm-bs3	480803 / 480823 / 480843
FMS-lg-bs1	480804 / 480824 / 480844
FMS-lg-bs2	480805 / 480825
FMS-lg-bs3	480806 / 480826

## 53 2.3 Calibration

54 The calibration for run 15 FMS dataset are from existing STAR framework [12],  
 55 but with some additional steps. They mainly include the following items:

- 56 • Bit shift (BS): It refers to the binary bit, used to store the ADC value,  
 57 not starting from the normal lowest bit. The BS will affect a cell's ADC  
 58 distribution and the corresponding hit energy. The approach to check the  
 59 BS is to use the ADC of each FMS hit to check with its corresponding BS  
 60 value of the cell [12].
- 61 • Gain and gain correction: The energy of the hit = ADC  $\times$  gain  $\times$  gain  
 62 correction. The gain is the calculated value based on a cell's  $\eta$  position,  
 63 while the gain correction is obtained from offline calibration [12]. The flag  
 64 of the gain and the gain correction for each tower in the STAR database  
 65 is "fmsGainCorr-BNL-C".
- 66 • Hot channel and bad channel masking: A hot channel refers to the tower  
 67 with a number of hits far more than the average number of hits for the  
 68 whole detector towers within some time range. A bad channel refers to  
 69 the problematic towers that might suffer from hardware issues. Both hot  
 70 and bad channels can affect the quality of the calibration and the analyses  
 71 since there are quite a lot of non-physical signals that are contaminated.  
 72 To mask out these channels, the gain values are set to zero. In addition to

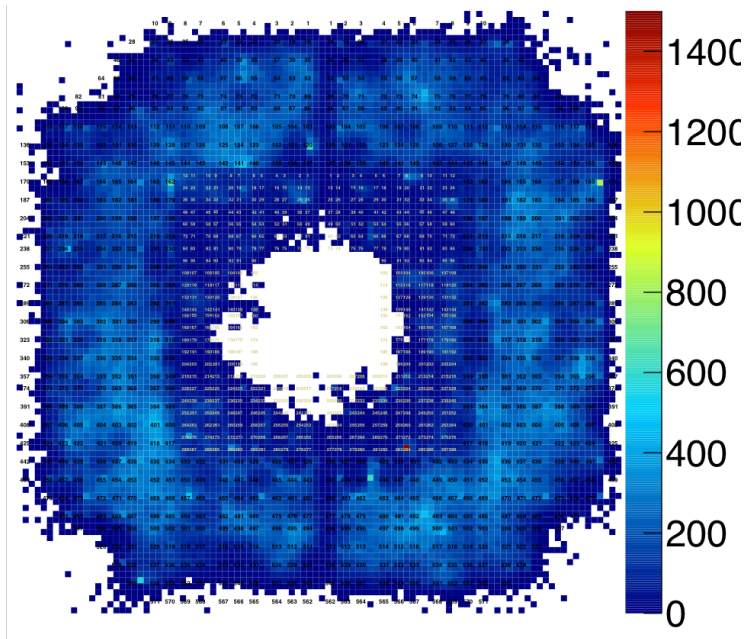


Figure 2.1: Example of EM-jet distribution at FMS before additional hot channel masking. The red color area in this plot indicates the possible hot channels.

73 the existing hot channel and bad channel masking from STAR calibration  
 74 [12], the fill-by-fill hot channel masking is applied in this analysis. The  
 75 EM-jet distribution before any event selections for every fill is checked to  
 76 find out any possible hot channels. The EM-jet reconstruction is discussed  
 77 in 3.1. Figure (2.1) shows one example of the EM-jet distribution at  
 78 the FMS. The areas with extremely high EM-jet entries compared to the  
 79 overall average entries in the plot are assumed to be the hot channel  
 80 area. The channels within these areas are considered hot channels and  
 81 added manually to the hot channel lists. Figure (2.2) shows the EM-jet  
 82 distribution for fill 18827 as an example after the additional hot channel  
 83 masking. From the plot, the hot channels disappear, and the majority of  
 84 towers have entries close to the average.

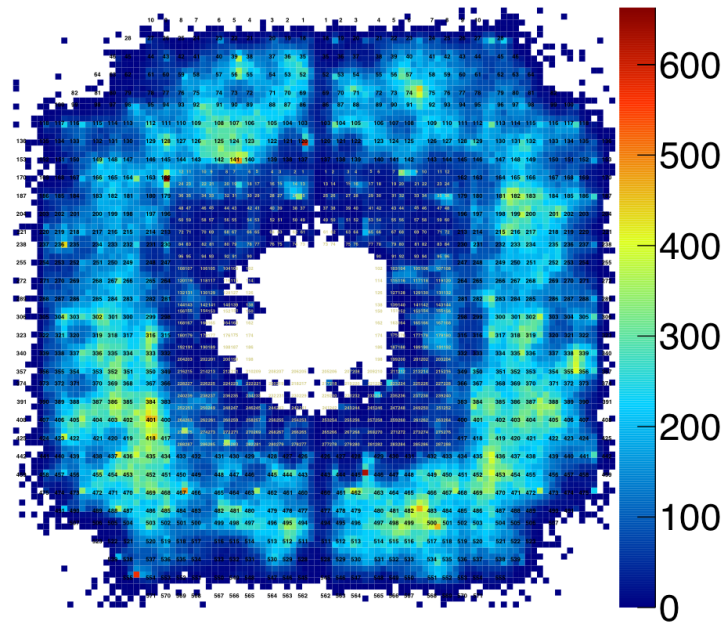


Figure 2.2: Example of EM-jet distribution at FMS after additional hot channel masking.

## Chapter 3

# Single Diffractive Process and Event Selection

One of the major characteristics of the diffractive processes is the presence of the rapidity gap. This analysis utilizes the proton track from east RP and the EM-jet at FMS, which allows for the large rapidity gap. Since there is only 1 proton in the final state process, this diffractive process is called the single diffractive process. The diagram for this process is shown in Fig. (3.1).

In order to determine the single diffractive process and minimize the effect of accidental coincidence events (AC) and pile-up events, the event selections and corrections include the following items:

1. Triggers: The triggers used for this analysis are the FMS BS triggers and FMS JP triggers. They are listed in Table(2.1). Only the events with any triggers fired are kept.
2. EM-jet cut: Details of the EM-jet cuts are in Section (3.1)
  - EM-jet reconstruction: EM-jets are reconstructed by FMS points

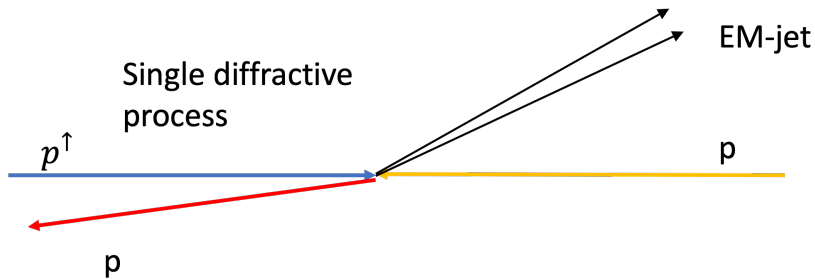


Figure 3.1: Diagram for single diffractive process.

- 101 using the Anti- $k_T$  algorithm with  $R = 0.7$ . The FMS points are  
102 required to have  $E > 1$  GeV and  $E_T > 0.2$  GeV.
- 103 • The EM-jets are required to have  $p_T > 2$  GeV and pass trigger  $p_T$   
104 threshold.
  - 105 • The pseudorapidity ( $\eta$ ) of the EM-jets is within [2.8, 3.8].
  - 106 • The event with EM-jet  $E > 100$  GeV are excluded.
  - 107 • The number of EM-jets for each event is 1.
  - 108 • Energy corrections for EM-jets: Underlying-Event (UE) correction  
109 (details in Sector(4.1) , and EM-jet energy correction (details in Sec-  
110 tor(4.2)) )
- 111 3. Event property cut: Details of the event property cuts are in Section (3.2)
- 112 • Veto on abort gap.
  - 113 • The spin status for the blue beam and yellow beam is correct and  
114 accepts the 4 cases of 4-bit spin patterns (Tab. (3.2)).
  - 115 • The vertex  $z$  is within [-80, 80] cm.
- 116 4. BBC East veto cut: Details of the BBC East veto cut are in Section (3.3).
- 117 • East BBC ADC sum cut: east side large BBC ADC sum  $< 80$  and  
118 east side small BBC ADC sum  $< 90$ .
- 119 5. Roman Pot (RP) track cut: Details are in Section (3.4)
- 120 • Only accept the event with exactly only one east side RP track.
  - 121 • The east RP track must hit at least 7 RP silicon planes.
  - 122 • East RP track  $\xi$  dependent  $\theta_X$ ,  $\theta_Y$ ,  $p_X$  and  $p_Y$  cuts.
  - 123 • East RP track  $\xi$  range:  $0 < \xi < 0.15$

### 124 3.1 Electromagnetic jet reconstruction and cuts

125 Electromagnetic jets (EM-jets) are jets consisting of only photons. The photon  
126 candidates for EM-jets reconstruction are the FMS points. The description of  
127 FMS points can be found in [14].

128 In order to reduce the noise background, only the FMS points with  $E > 1$   
129 GeV are applied to the EM-jet reconstruction. The EM-jets are reconstructed  
130 with the anti- $k_T$  algorithm from the FastJet package [13], with the resolution  
131 parameter  $R = 0.7$ . The primary vertex of the EM-jets is determined according  
132 to the priority of the TPC vertex, VPD vertex, and BBC vertex. If the primary



133 vertex cannot be determined among these three detectors, it will be set to be  
 134 (0,0,0). The EM-jet transverse momentum ( $p_T$ ) is required to pass the trigger  
 135 threshold and the fixed threshold 2 GeV/ $c$  threshold. The trigger thresholds are  
 136 listed in Table (3.1). All of them have a 15% increase compared to the original  
 137 trigger threshold setup.

138 The EM-jet vertex is determined by the primary vertex following the priority  
 139 of TPC, VPD, and BBC. If the primary vertex can be obtained by TPC, the  
 140 TPC vertex will be the primary vertex. Otherwise, check the VPD vertex on the  
 141 next step. If there is no VPD vertex, then check the BBC vertex. If there is still  
 142 no BBC vertex, the primary vertex is set to be  $z=0$ . The fraction of the vertex  
 143  $z$  obtained from TPC, VPD, and BBC are 1%, 33%, and 50%, respectively. The  
 144 vertex  $z$  cut on  $|z| < 80$  cm is considered.

145 In addition, we apply the cut on EM-jet pseudorapidity ( $\eta$ ), which aims to  
 146 get rid of the badly reconstructed EM-jets and the EM-jets hitting outside the  
 147 FMS. Therefore, the  $\eta$  of the EM-jet cut is required to be within [2.8, 3.8].

148 Also, the events with EM-jet energy  $E > 100$  GeV or  $|x_F| > 1$  are discarded,  
 149 where Feynman- $x$   $x_F$  can be estimated by the EM-jet energy divided by the  
 150 beam energy ( $x_F = \frac{2E}{\sqrt{s}}$ ). These events are about 0.17% of the entire dataset.  
 151 Those events with these unreasonable EM-jets are possibly pile-up events.

152 The general raw EM-jet  $p_T$  vs energy distribution is shown in Fig. (3.2).

153 Finally, the number of EM-jets in each event is required to be only one. This  
 154 can satisfy the requirement for single diffractive events and minimize the effect  
 155 of the pile-up events. Figure (3.3) shows the number of EM-jets distribution,  
 156 about 92% of the events are containing only one EM-jet at FMS.

## 157 3.2 Event property cut

158 The abort gap for both blue beam and yellow beam is within bunch ID [31, 39]  
 159 and [111, 119] for run 15. The events with either blue beam or yellow beam  
 160 with the abort gap are discarded.

161 The spin patterns for each beam, either up or down, are obtained from the  
 162 bunch crossing of each event. The translation from the database for the spin  
 163 patterns is described in Tab. (3.2). The spin patterns for both blue and yellow  
 164 beam are combined as 4-spin bit. The events satisfying the following 4 4-spin  
 165 bit cases in Table (3.2) are considered in this analysis. These patterns require  
 166 the polarizations of both blue and yellow beam are either up or down.

Trigger name	Trigger ID	15% increase $p_T$ cut [GeV]
FMS-JP0	480810 / 480830	1.84
FMS-JP1	480809 / 480829	2.76
FMS-JP2	480808 / 480828	3.68
FMS-sm-bs1	480801	1.26
FMS-sm-bs1	480821 / 480841	1.15
FMS-sm-bs2	480802 / 480822	1.84
FMS-sm-bs3	480803	2.53
FMS-sm-bs3	480823 / 480843	2.18
FMS-lg-bs1	480804	1.26
FMS-lg-bs1	480824 / 480844	1.15
FMS-lg-bs2	480405 / 480425	1.84
FMS-lg-bs3	480406 / 480426	2.76

Table 3.1: EM-jet trigger threshold  $p_T$  cut, listed by trigger name and trigger ID.

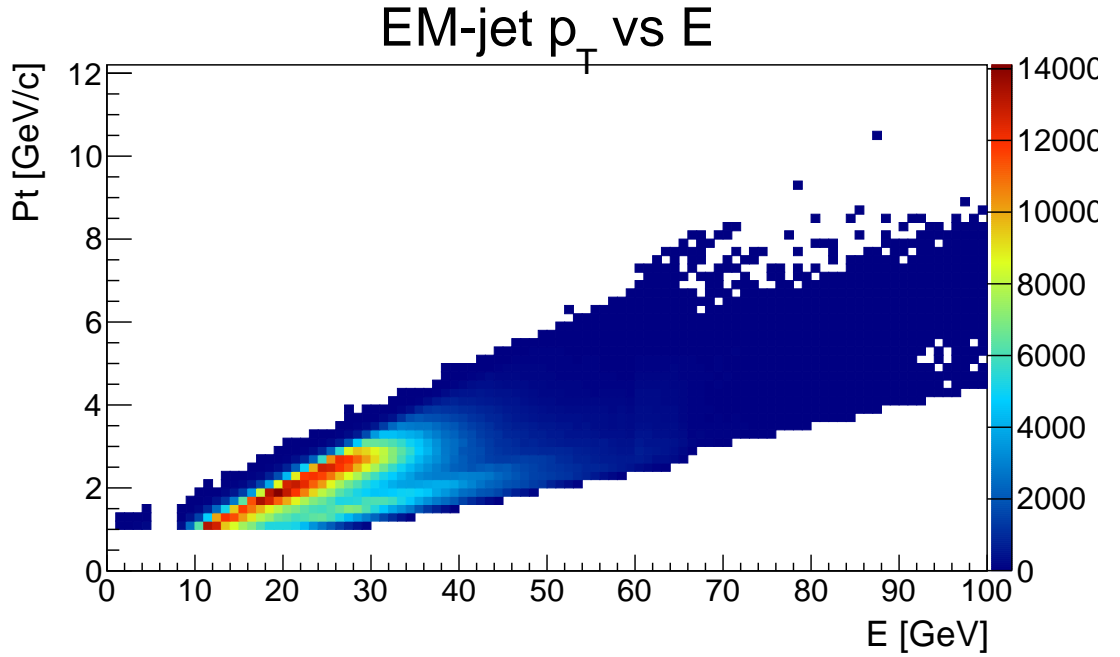


Figure 3.2: EM-jet transverse momentum ( $p_T$ ) vs energy (E) before correction.

## Number of EM-jets

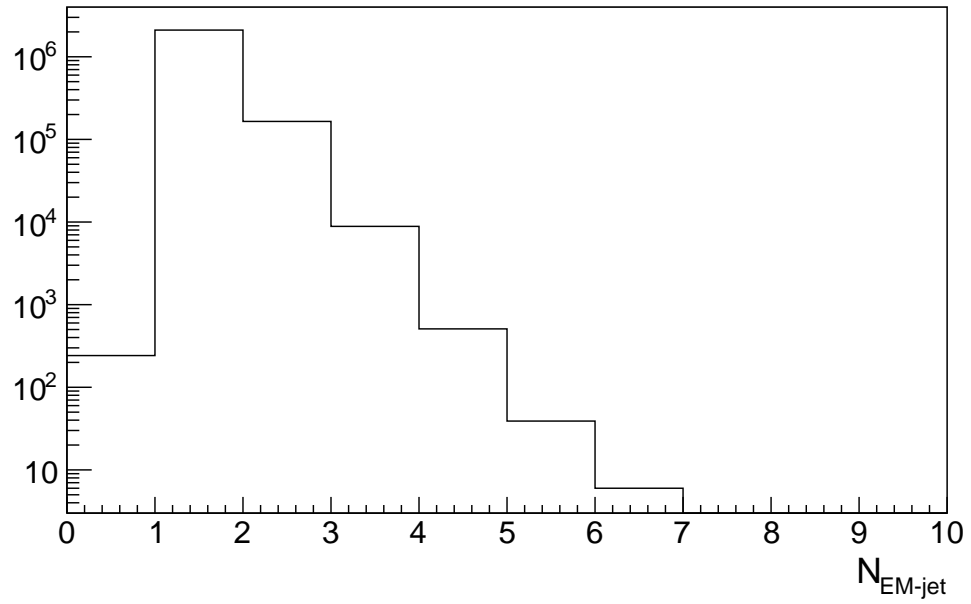


Figure 3.3: Number of EM-jets in the event.

Table 3.2: 4 acceptable 4-bit spin patterns

4-bit spin	Translate	Blue beam polarization	Yellow beam polarization
0101	5	up	up
0110	6	up	down
1001	9	down	up
1010	10	down	down

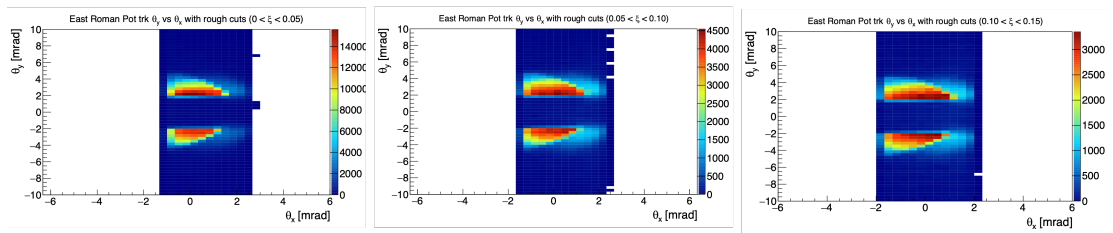


Figure 3.4: East RP  $\theta_X$  and  $\theta_Y$  distributions for 7 different East RP track  $\xi$  ranges with only applying East BBC ADC sum  $< 150$ .

### 167 3.3 BBC East veto cut

168 The major goal for the BBC East veto cut is to minimize accidental coincidence  
 169 events (AC), also called multiple collision events. Furthermore, it helps to ensure  
 170 the rapidity gap requirement for the single diffractive process since the BBC East  
 171 detector covers  $-5 < \eta < -2.1$ .

172 The study of BBC East veto cuts is carried out simultaneously with the East  
 173 RP track cut study. To begin with, the rough cut on a small BBC East ADC  
 174 sum  $< 150$  is applied to get rid of some of the backgrounds because the events  
 175 with high BBC East ADC sum are more likely to be AC events. Then, with  
 176 the rough BBC East ADC sum cut, the East RP  $\theta_X$  and  $\theta_Y$  distributions for  
 177 East RP track with different  $\xi$  ranges are checked, where  $\xi$  is the fraction of  
 178 proton momentum loss in the collision. The goal of checking the rough East  
 179 RP  $\theta_X$  and  $\theta_Y$  distributions is to figure out the rough East RP  $\theta_X$  and  $\theta_Y$   
 180 cuts and use them to further checking the proper small/large BBC East ADC  
 181 sum distribution to determine the BBC East veto cuts. Figure (3.4) shows the  
 182 rough East RP  $\theta_X$  and  $\theta_Y$  distributions for 7 different East RP  $\xi$  regions. From  
 183 the hot areas for every single figure, which are shown in red and yellow color,  
 184 we determine the rough cut for East RP  $\theta_X$  and  $\theta_Y$ . The rough East RP  $\theta_Y$   
 185 cuts are:  $2.0 < |\theta_Y| < 4.0$  mrad, and The rough East RP  $\theta_X$  cuts are shown  
 186 in Tab. (3.3). Then, with the rough East RP  $\theta_X$  and  $\theta_Y$  cuts applied, we  
 187 explore the small/large east BBC ADC sum distributions to determine the cuts  
 188 on small/large east BBC cuts. The left panel of Fig. (3.5) shows the small east  
 189 BBC ADC sum distribution, while the right panel of Fig. (3.5) shows the large  
 190 east BBC ADC sum distribution. According to Fig. (3.5), we decide the small  
 191 BBC east ADC sum  $< 90$  and the large BBC east ADC sum  $< 80$ .

### 192 3.4 Roman Pot track cut

193 The proton track is detected from the RP detector, where the description of the  
 194 RP detector can be found in [15]. For this analysis, we only accept the case with

$\xi$ range	$\theta_X$ rough cuts [mrad]
$0.00 < \xi < 0.05$	$-1.0 < \theta_X < 1.5$
$0.05 < \xi < 0.10$	$-1.25 < \theta_X < 1.25$
$0.10 < \xi < 0.15$	$-1.5 < \theta_X < 1.25$
$0.15 < \xi < 0.20$	$-2.0 < \theta_X < 0.75$
$0.20 < \xi < 0.25$	$-2.5 < \theta_X < 0.75$
$0.25 < \xi < 0.30$	$-3.0 < \theta_X < 0.5$
$0.30 < \xi < 0.50$	$-5.0 < \theta_X < -0.25$

Table 3.3: Rough cuts for East RP track  $\theta_X$  by different East RP track  $\xi$

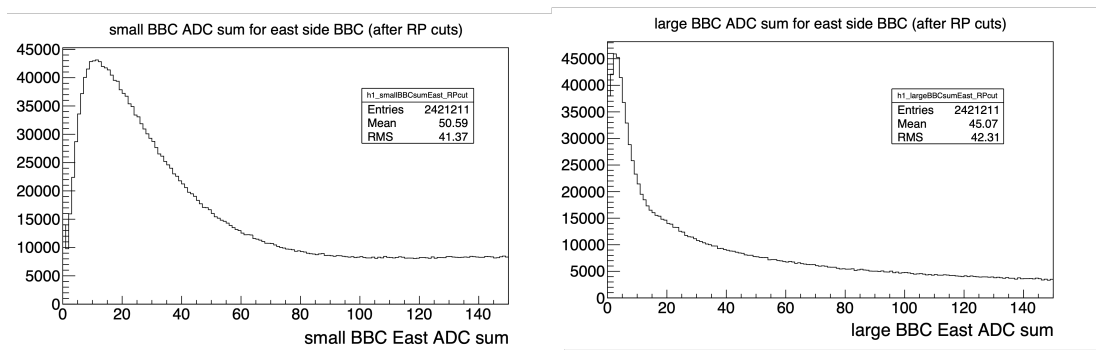


Figure 3.5: The small (left) and large (right) East BBC ADC sum distribution after the rough East RP  $\theta_X$  and  $\theta_Y$  cuts

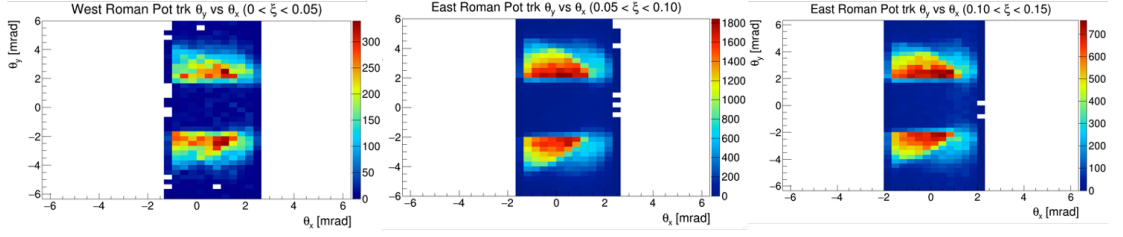


Figure 3.6: East RP  $\theta_X$  and  $\theta_Y$  distributions for three East RP track  $\xi$  ranges.

$\xi$ range	$\theta_X$ final cuts [mrad]
$0.00 < \xi < 0.05$	$-1.0 < \theta_X < 1.5$
$0.05 < \xi < 0.10$	$-1.25 < \theta_X < 1.25$
$0.10 < \xi < 0.15$	$-1.5 < \theta_X < 1.25$

Table 3.4: Final cuts for East RP track  $\theta_X$  by three  $\xi$  regions

195 only one East RP track detected. To ensure the RP track is well reconstructed,  
 196 the RP track must hit at least 7 RP silicon planes. Also, the BBC East veto  
 197 cuts (details in Sec. (3.3)) are also applied to explore the East RP track cuts.  
 198 Furthermore, according to the Particle Data Book [16], the proton  $\xi$  for the  
 199 diffractive process should be less than 0.15. Therefore, the cut on East RP  
 200 track  $0 < \xi < 0.15$  is also applied. With all of these cuts applied, first of all,  
 201 the East RP track  $\theta_X$  and  $\theta_Y$  distributions are further explored. Figure (3.6)  
 202 shows the East RP track  $\theta_X$  and  $\theta_Y$  distributions for three  $\xi$  ranges. The hot  
 203 area will be considered as acceptable final East RP  $\theta_X$  and  $\theta_Y$  cuts. The final  
 204 East RP track  $\theta_Y$  cuts are uniform for all three  $\xi$  ranges:  $2 < |\theta_Y| < 4$  mrad.  
 205 However, the final East RP track  $\theta_X$  cuts are  $\xi$  dependent, shown in Tab. (3.4).  
 206 Finally, with then the final East RP  $\theta_X$  and  $\theta_Y$  cuts applied, the East RP track  
 207  $p_X$  and  $p_Y$  distributions are also explored to study their cuts. The idea is the  
 208 same as investigating the East RP track  $\theta_X$  and  $\theta_Y$  cuts. Figure (3.7) shows  
 209 the East RP track  $p_X$  and  $p_Y$  distributions for three  $\xi$  ranges. The shape of a  
 210 rectangle with a quarter circle is used to describe the final East RP track  $p_X$   
 211 and  $p_Y$  cuts. The expressions are detailed in Tab. (3.5).

212 In summary, the cuts on East RP track include all the following: Number  
 213 of RP Silicon planes hits greater than 6;  $0 < \xi < 0.15$ ; East RP track  $\theta_X$  and  
 214  $\theta_Y$  cuts; East RP track  $p_X$  and  $p_Y$  cuts.

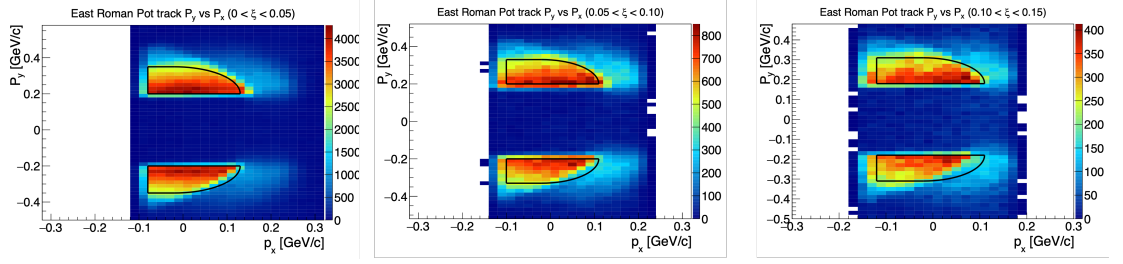


Figure 3.7: East RP track  $p_X$  and  $p_Y$  distributions for three East RP track  $\xi$  ranges. The black curves indicate the ranges of accepted East RP track  $p_X$  and  $p_Y$  cuts.

$\xi$ range	$p_X$ and $p_Y$ final cuts [GeV/c]
$0.00 < \xi < 0.05$	$(p_X + 0.02)^2 + ( p_Y  - 0.2)^2 < 0.15^2$ or $-0.08 < p_X < -0.02$ and $0.2 <  p_Y  < 0.35$
$0.05 < \xi < 0.10$	$(p_X + 0.02)^2 + ( p_Y  - 0.2)^2 < 0.13^2$ or $-0.10 < p_X < -0.02$ and $0.2 <  p_Y  < 0.33$
$0.10 < \xi < 0.15$	$(p_X + 0.02)^2 + ( p_Y  - 0.18)^2 < 0.13^2$ or $-0.12 < p_X < -0.02$ and $0.18 <  p_Y  < 0.31$

Table 3.5: East RP track  $p_X$  and  $p_Y$  final cuts

## 215 Chapter 4

# 216 Corrections

### 217 4.1 Underlying Event (UE) correction

218 The underlying event contribution is part of a jet, not from the parton fragmen-  
219 tation but from secondary scattering or other processes. This will deposit some  
220 energy into the jet, so the correction on UE is required to subtract its energy  
221 from the jet. The "off-axis" method [17] is used. In this method, first of all,  
222 two off-axis jets with the same pseudorapidity but at  $\pm\pi/2$  azimuthal angle at  
223 the edge of the original jet are reconstructed as UE background. Then, the UE  
224 energy density ( $\rho$ ) can be calculated using  $\rho = E/(\pi R^2)$ , where E is the average  
225 UE energy and R is the UE jet radius. The fastjet program uses the "ghost  
226 particle" technique to calculate the jet area (A). The maximum "ghost particle"  
227  $\eta$  is 5.0, and the "ghost area" is 0.04. Finally, the jet energy will be subtracted  
228 by the UE energy:  $E_{corrected} = E_{original} - \rho \times A$ , where the corrected EM-jet  
229 energy is  $E_{corrected}$ , and the original EM-jet energy is  $E_{original}$ .

230 Figure (4.1) shows the UE correction distribution for EM-jet energy. The  
231 left plot shows the subtraction term for the UE correction for EM-jet energy.  
232 The right plot shows the EM-jet energy distribution after the UE correction. If  
233 the EM-jet energy after subtraction is less than 0 GeV, the energy will be set  
234 to 0 GeV.

### 235 4.2 Detector level to particle level EM-jet en- 236 ergy correction

237 The EM-jet energy obtained from FMS is considered detector-level EM-jet en-  
238 ergy. Therefore, a correction for detector level to particle level EM-jet energy is  
239 necessary. The correction is based on the Monte Carlo simulation for FMS. For



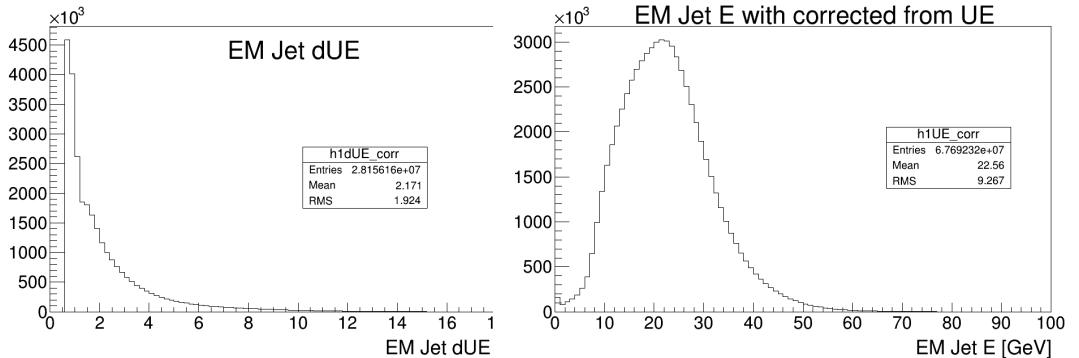


Figure 4.1: UE distribution for diffractive EM-jet analysis. The left plot shows the subtraction term  $\rho \times A$ . The right plot shows the EM-jet energy distribution after the UE correction.

240 the PYTHIA simulation, the proton-proton collisions with  $\sqrt{s} = 200$  GeV are  
 241 generated, with the tune setting of Perugia2012 (Tune parameter 370) [18, 19].  
 242 Then, the GEANT3 with FMS detector response implemented under STAR  
 243 simulation framework ("starsim") is used for the FMS simulation. The Big  
 244 Full Chain (BFC) proceeds with the event reconstruction. The chain options  
 245 are "ry2015a agml usexgeom MakeEvent McEvent vfmce Idst BAAna l0 l3 Tree  
 246 logger fmsSim fmspoint evout -dstout IdTruth bigbig fzin geantout clearmem  
 247 sdt20150417.193427". The EM-jet reconstruction is proceeded along with the  
 248 BFC process. The Anti- $k_T$  algorithm with  $R=0.7$  is used for the EM-jet recon-  
 249 struction, the same as the EM-jet reconstruction for data.

250 For the simulation results, the EM-jets with both particle level and detector  
 251 level are recorded. Figure (4.2) shows the EM-jet energy distribution in particle  
 252 level (y-axis) and detector level (x-axis). Figure (4.3) shows the profile of the  
 253 EM-jet energy distribution with particle level and detector level. The black  
 254 points are the correlation between the EM-jet energy at the particle level and  
 255 detector level. The red curves are fit for the points in two different detector level  
 256 regions:  $5 < E < 10$  GeV and  $10 < E < 60$  GeV. The 6th-order polynomial  
 257 function is used for fitting the former region and the linear function is used for  
 258 fitting the latter region. The parameters of the 6th-order polynomial are shown  
 259 in Tab. (4.1), while the linear function is:  $E_{par} = 1.07 * E_{det} + 1.13$ , where  
 260  $E_{par}$  is the particle level EM-jet energy and  $E_{det}$  is the detector level EM-jet  
 261 energy. These functions are used to calculate the corrected energy from the  
 262 original detector level energy. The corrected EM-jet energy will finally applied  
 263 for the  $x_F$  calculation and  $A_N$  extraction.

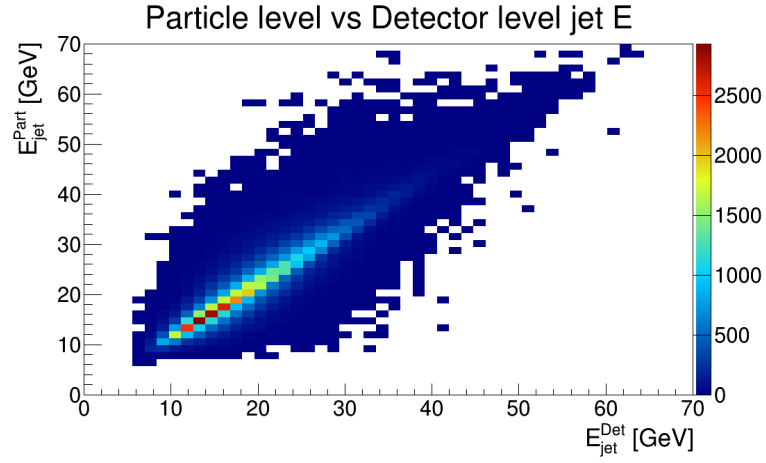


Figure 4.2: EM-jet energy distribution in particle level (y-axis) and detector level (x-axis) from the FMS simulation.

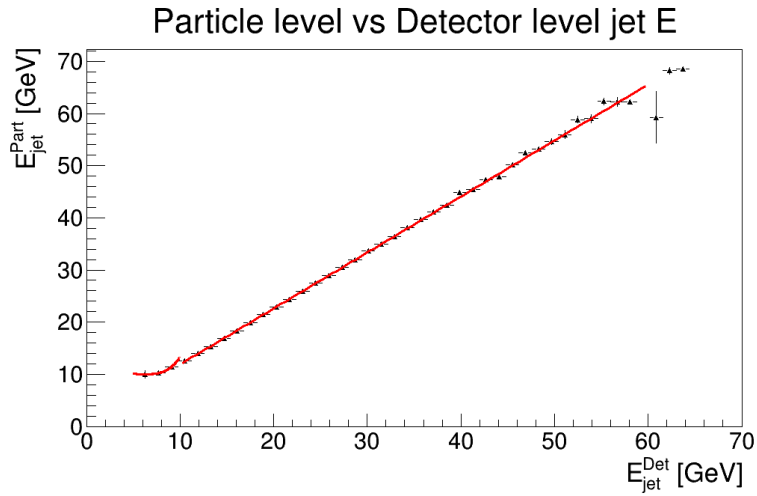


Figure 4.3: The profile of the EM-jet energy distribution with particle level and detector level. The black points are the correlation between the EM-jet energy at the particle level and detector level. The red curves are the fit for the black points.

[0]	[1]	[2]	[3]	[4]	[5]	[6]
8.93e0	-6.64e-1	1.51e-1	-6.66e-3	1.56e-4	-1.85e-6	8.65e-9

Table 4.1: Parameters for the 6th-order polynomial

## 264 Chapter 5

# 265 Rapidity Gap (RG) events 266 study

### 267 5.1 Motivation

268 The rapidity gap (RG) events are also within our interest in studying the po-  
269 tential background for the single diffractive events. The RG events are the type  
270 of events coinciding with FMS EM-jets and East BBC veto, with the schematic  
271 diagram shown in Fig. (5.1). The details description for the FMS EM-jets and  
272 east BBC veto are in Sec. (5.2). Since there is no requirement on the RP track  
273 (proton) on any side, the RG events are considered as the subset of the inclu-  
274 sive events, and they can also serve as additional enrichment for the inclusive  
275 process. According to the Pythia 8 simulation for hard QCD process (can be  
276 considered as non-single diffractive events) and the single diffractive events, the  
277 east BBC veto cuts are able to cut out about 84% of the non-single diffractive  
278 events, but just cut out about 14% of the single diffractive events with a proton  
279 on the east side. Therefore, such a process can help separate the diffractive  
280 and non-diffractive processes with the rapidity gap requirement. Studying the  
281 RG events can allow us to investigate the single diffractive process without the  
282 effects on the limited Roman Pot acceptance for tagging the scattered proton.

### 283 5.2 Event selection for RG events

284 The dataset used for the RG events is the same as single diffractive events,  
285 shown in Sec. (2.1). The event selection criteria of the FMS EM-jets, event  
286 property cuts, and the East BBC veto for the RG events are the same as those  
287 for the single diffractive events, which are shown in Sec. (3.1), Sec. (3.2) and

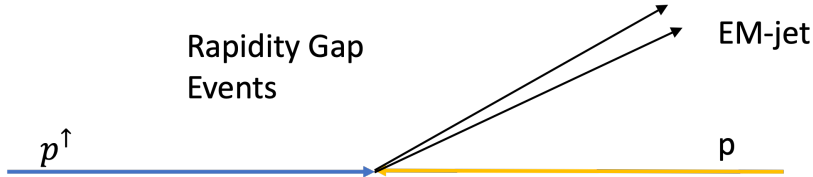


Figure 5.1: Diagram for rapidity gap events.

288 Sec. (3.3), respectively. The idea behind choosing the same FMS EM-jet cuts  
 289 and East BBC veto cuts is to make them consistent and comparable to the  
 290 single diffractive process.

### 291 5.3 Fraction of single diffractive events in rapid- 292 ity gap events

293 The study on the fraction of single diffractive events in rapidity gap events in  
 294 data can be measured using the simulation. The simulation is using the Pythia  
 295 8 single diffractive process (SoftQCD:singleDiffractive). Both the east BBC  
 296 detector simulation (via GEANT3 based STAR detector level simulation) and  
 297 the east RP detector simulation (via pp2pp simulation [25]) are used for the  
 298 simulation study. The same east BBC veto (detailed in Sec. (3.3)) is applied  
 299 in the simulation to determine the veto on the east BBC region (rapidity gap)  
 300 as well. The cut on the east RP track hitting more than 6 east RP planes is  
 301 used for determining the good east RP track. In addition, only one RP track is  
 302 allowed as the east RP cut for the single diffractive events.

303 Based on the criteria above, we define the single diffractive events (SD) in  
 304 the simulation as the events passing the east BBC veto and the east RP cut.  
 305 Also, we define the rapidity gap events (RG) in the simulation as the events  
 306 passing the east RP cut without requirement on the east RP cut. The RG  
 307 events in simulation are all real single diffractive events (RSD). The definition  
 308 of single diffractive events and rapidity gap events in data are the same as  
 309 mentioned in previous sections. However, the RG events in data contain real  
 310 single diffractive events (RSD) and non-single diffractive events (NSD). When  
 311 we calculate the fraction of single diffractive events to the rapidity gap events in  
 312 simulation and data, the equation for simulation and data can be expressed as  
 313 Equ. (5.1) and Equ. (5.2), respectively. In the calculation,  $frac(sim) = 16.03\%$   
 314 and  $frac(data) = 11.08\%$ . Since the purity of the single diffractive events in  
 315 data is high, we can consider the fraction of single diffractive events (SD) to  
 316 the real single diffractive events in rapidity gap event (RSD),  $\frac{SD}{RSD}$ , is same

317 between data and simulation. Considering the major systematic uncertainty  
318 of the fraction comes from the uncertainty of BBC detector (6.5%) [26] and  
319 RP detector (10%) [25]. The SD fraction in RG events in data ( $\frac{RSD}{RSD+NSD}$ ) is  
320  $68.7\% \pm 0.6\% \pm 8.2\%$ .

$$frac(sim) = \frac{SD}{RSD} \quad (5.1)$$

$$frac(data) = \frac{SD}{RSD + NSD} \quad (5.2)$$

## 321 Chapter 6

# 322 Semi-exclusive process 323 study

324 The semi-exclusive process requires only one EM-jet at FMS and one proton  
325 detected in west side RP. The event selections of the EM-jet are same as that  
326 used in single diffractive process and rapidity gap events, showing in Sec. 3.1.  
327 Additionally, an exclusive constraint on the sum of the energy of the EM-jet  
328 and the west RP track (energy sum) is applied. It requires the energy sum are  
329 same as proton beam energy within resolution. Therefore, this process is termed  
330 as semi-exclusive process. The schematic diagram for semi-exclusive process is  
331 shown in Fig. (6.1).

332 In order to determine the single diffractive process and minimize the effect  
333 of accidental coincidence events (AC) and pile-up events, the event selections  
334 and corrections include the following items:

- 335 1. Triggers: The triggers used for this analysis are the FMS BS triggers and  
336 FMS JP triggers. They are listed in Table(2.1). Only the events with any  
337 triggers fired are kept.



Figure 6.1: Diagram for semi-exclusive process.

- 338 2. EM-jet cut: Details of the EM-jet cuts are in Section (3.1) These cuts are  
339 same as that in single diffractive process and rapidity gap events.
- 340 • EM-jet reconstruction: EM-jets are reconstructed by FMS points  
341 using the Anti- $k_T$  algorithm with  $R = 0.7$ . The FMS points are  
342 required to have  $E > 1$  GeV and  $E_T > 0.2$  GeV.
  - 343 • The EM-jets are required to have  $p_T > 2$  GeV and pass trigger  $p_T$   
344 threshold.
  - 345 • The pseudorapidity ( $\eta$ ) of the EM-jets is within  $[2.8, 3.8]$ .
  - 346 • The event with EM-jet  $E > 100$  GeV are excluded.
  - 347 • The number of EM-jets for each event is 1.
  - 348 • Energy corrections for EM-jets: Underlying-Event (UE) correction  
349 (details in Sector(4.1) , and EM-jet energy correction (details in Sec-  
350 tor(4.2)) )
- 351 3. Event property cut: Details of the event property cuts are in Section (3.2)
- 352 • Veto on abort gap.
  - 353 • The spin status for the blue beam and yellow beam is correct and  
354 accepts the 4 cases of 4-bit spin patterns (Tab. (3.2)).
  - 355 • The vertex z is within  $[-80, 80]$  cm.
- 356 4. BBC West veto cut: Details of the BBC West veto cut are in Section (6.1).
- 357 • West BBC ADC sum cut: west side large BBC ADC sum  $< 60$  and  
358 west side small BBC ADC sum  $< 80$ .
- 359 5. Roman Pot (RP) track cut: Details are in Section (6.2)
- 360 • Only accept the event with exactly only one west side RP track.
  - 361 • The west RP track must hit at least 7 RP silicon planes.
  - 362 • West RP track  $\xi$  dependent  $\theta_X, \theta_Y, p_X$  and  $p_Y$  cuts.
  - 363 • West RP track  $\xi$  range:  $0 < \xi < 0.45$
- 364 6. Energy sum cuts: Sum of the energy of west RP track and EM-jet is  
365 required to be equal to the beam energy, within the resolution.

## 366 6.1 West BBC veto cuts

367 The major goal for the BBC West veto cut is to minimize accidental coincidence  
368 events (AC), which are called multiple collision events. However, the west BBC

West RP $\xi$ range	West RP $\theta_X$ rough cut [mrad]
$0 < \xi < 0.05$	$-1 < \theta_X < 1.75$
$0.05 < \xi < 0.1$	$-1.5 < \theta_X < 1.5$
$0.1 < \xi < 0.15$	$-1.75 < \theta_X < 1.25$
$0.15 < \xi < 0.2$	$-2.5 < \theta_X < 1.25$
$0.2 < \xi < 0.25$	$-3 < \theta_X < 1$
$0.25 < \xi < 0.3$	$-3.25 < \theta_X < 0.5$
$0.3 < \xi < 0.35$	$-3.75 < \theta_X < 0$
$0.35 < \xi < 0.4$	$-4.25 < \theta_X < -0.5$
$0.4 < \xi < 0.45$	$-5 < \theta_X < -1$

Table 6.1: Rough west RP  $\theta_X$  cuts

369 coverage is partially overlapped with the FMS coverage. Therefore, this west  
370 BBC veto can not provide enough size of rapidity gap to satisfy the requirement  
371 of the diffractive process.

372 The idea for determining the west BBC veto cuts are similar as for deter-  
373 mining the east BBC veto cuts. To begin with, the rough cuts on west RP  $\theta_X$   
374 and  $\theta_Y$  are applied to check the small BBC west ADC sum distribution. The  
375 distribution of west RP  $\theta_Y$  vs  $\theta_X$  are showing in Fig.(6.2), with the rough cut  
376 on west small BBC ADC sum  $< 150$ . From the plots, we determine the rough  
377 west RP  $\theta_Y$  cut on:  $1.5 < |\theta_Y| < 4$  mrad, with the rough west RP  $\theta_X$  cuts are  
378 listed in Tab. (6.1).

379 With these rough west RP  $\theta_X$  and  $\theta_Y$  cuts, the small BBC west ADC sum  
380 and the large BBC west ADC sum distributions are then checked. Figure (6.3)  
381 shows the small BBC west ADC sum, and Fig. (6.4) shows the large BBC west  
382 ADC sum. From the plots, we apply the cuts on small BBC west ADC sum  $<$   
383 80 and large BBC west ADC sum  $< 60$ .

## 384 6.2 Roman Pot (RP) track cut

385 The proton track for semi-exclusive process is detected from the west side RP  
386 detector. Only one west side RP track is accepted for this process, with no  
387 constrain on east side tracks. In addition, this west side RP track requires to  
388 hit more than 6 planes. The first set of cuts are the west RP  $\theta_X$  and  $\theta_Y$  cuts.  
389 Before exploring these cuts, the west BBC veto cuts are applied. Figure (6.5)  
390 shows the final distribution of west RP  $\theta_Y$  vs  $\theta_X$ . From the distributions, we



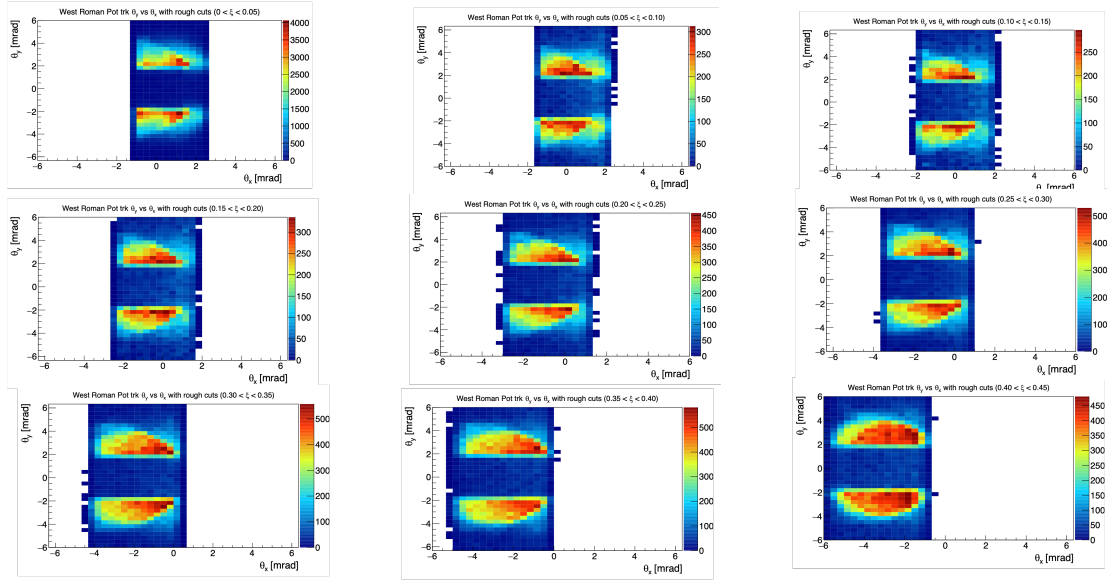


Figure 6.2: West RP  $\theta_X$  and  $\theta_Y$  distributions for 9 different East RP track  $\xi$  ranges with only applying West BBC ADC sum  $< 150$ .

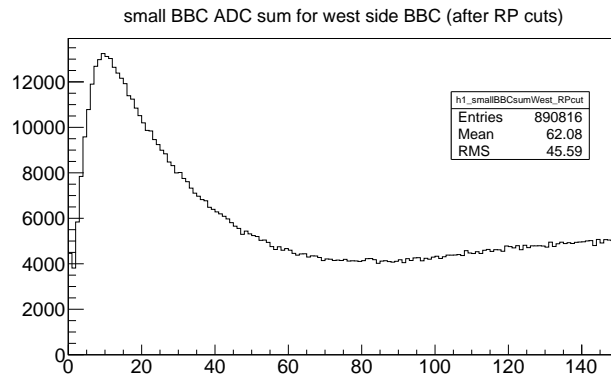


Figure 6.3: Small BBC west ADC sum distribution after the rough west RP cuts.

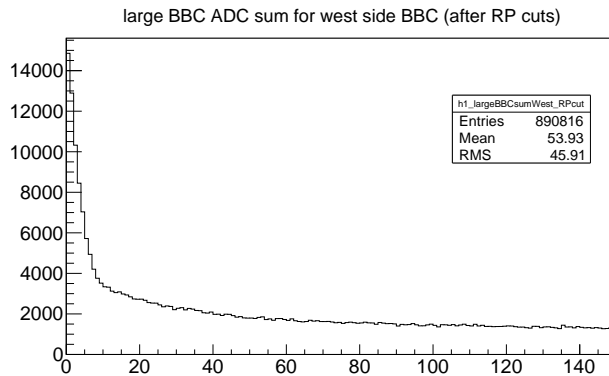


Figure 6.4: Large BBC west ADC sum distribution after the rough west RP cuts.

391 determine the  $\theta_Y$  cuts on:  $1.5 < |\theta_Y| < 4$  [mrad] ; and the  $\theta_X$  cuts shown in  
 392 Tab. (6.2). Then, with applying the west RP  $\theta_X$  and  $\theta_Y$  cuts, the west RP  $p_X$   
 393 and  $p_Y$  cuts are explored. Figure (6.6) shows the final distribution of west RP  
 394  $\theta_X$  and  $\theta_Y$  with the black curve region indicating the ranges of the cuts. The  
 395 cut values are shown in Tab. (6.3).

### 396 6.3 Energy sum cuts

397 For the semi-exclusive process, the final state includes the EM-jet and the pro-  
 398 ton. Both are on the same side (west side). Therefore, an exclusive constrain  
 399 on the sum of the energy for EM-jet and the proton should be consistent with  
 400 the beam energy within resolution. This is the reason for naming this process  
 401 as semi-exclusive process.

402 The energy sum cuts are explored with applying the west BBC veto cuts  
 403 and the west RP cuts. They are shown with EM-jet  $x_F$  dependent in Fig. (6.7).  
 404 and in Tab. (6.4).

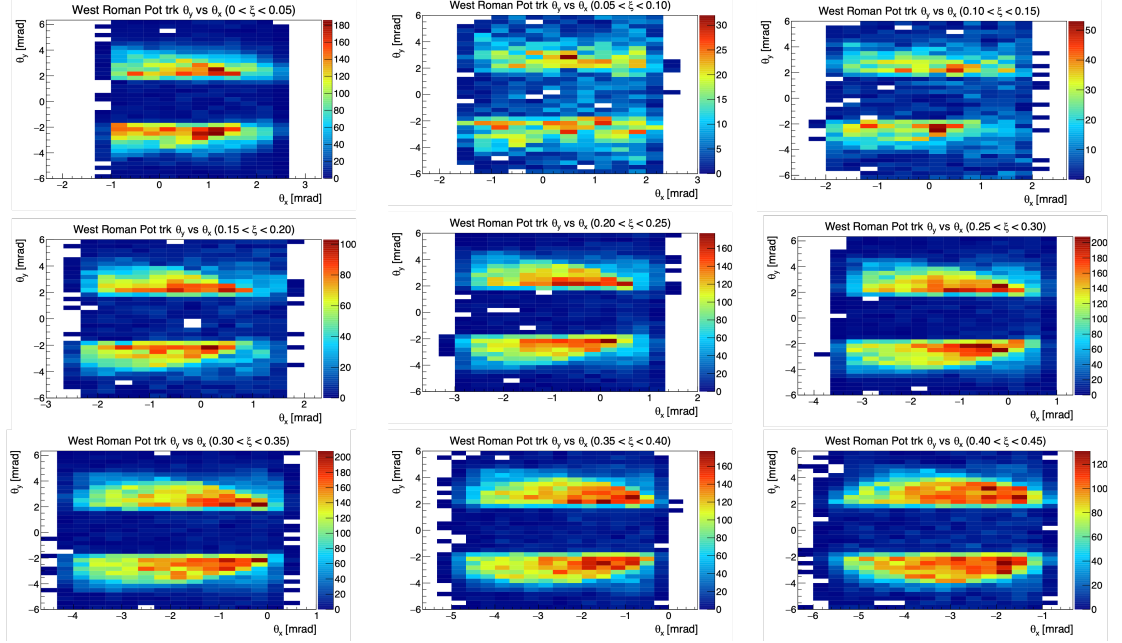


Figure 6.5: West RP  $\theta_X$  and  $\theta_Y$  distributions for 9 different East RP track  $\xi$  ranges after applying West BBC veto cuts.

West RP $\xi$ range	West RP $\theta_X$ final cut [mrad]
$0 < \xi < 0.05$	$-1 < \theta_X < 1.75$
$0.05 < \xi < 0.1$	$-1.5 < \theta_X < 1.5$
$0.1 < \xi < 0.15$	$-1.75 < \theta_X < 1.25$
$0.15 < \xi < 0.2$	$-2 < \theta_X < 1$
$0.2 < \xi < 0.25$	$-2.75 < \theta_X < 0.5$
$0.25 < \xi < 0.3$	$-3.25 < \theta_X < 0.5$
$0.3 < \xi < 0.35$	$-3.75 < \theta_X < 0$
$0.35 < \xi < 0.4$	$-4.5 < \theta_X < -0.5$
$0.4 < \xi < 0.45$	$-5.5 < \theta_X < -1.25$

Table 6.2: Final west RP  $\theta_X$  cuts

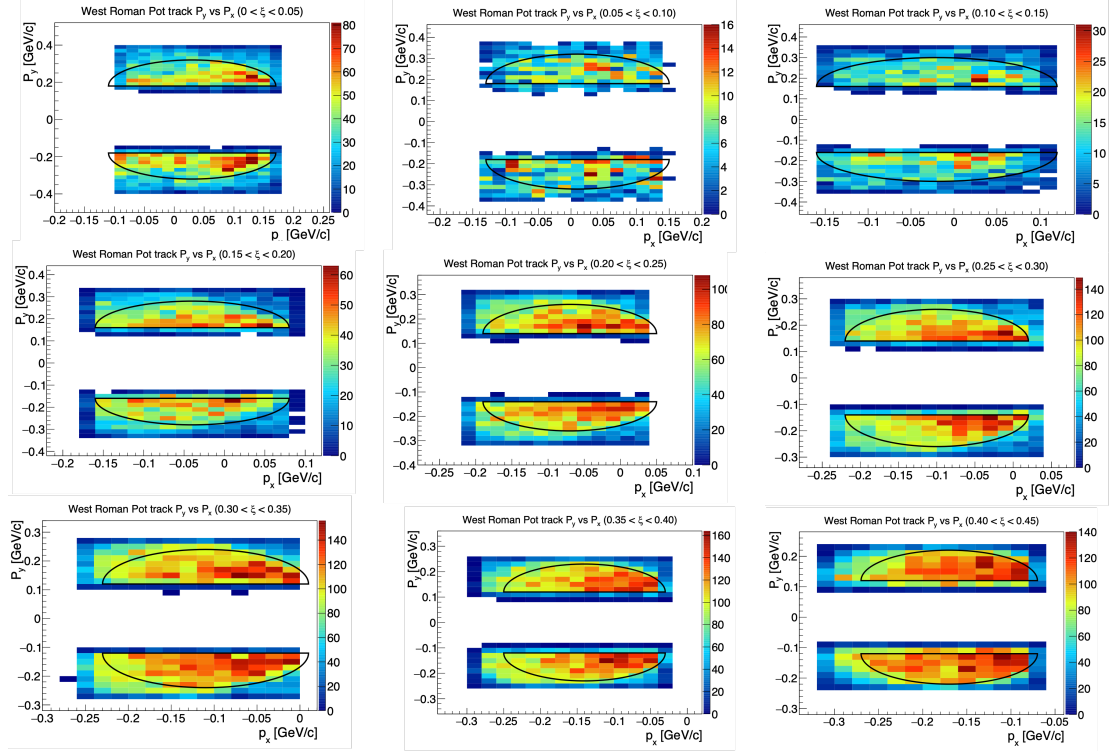


Figure 6.6: West RP track  $p_X$  and  $p_Y$  distributions for nine West RP track  $\xi$  ranges. The black curves indicate the ranges of accepted West RP track  $p_X$  and  $p_Y$  cuts.

West RP $\xi$ range	West RP $p_X$ and $p_Y$ final cut [GeV/c]
$0 < \xi < 0.05$	$(p_X - 0.03)^2 + (p_Y - 0.18)^2 < 0.14^2$ and $0.18 <  p_Y  < 0.32$
$0.05 < \xi < 0.1$	$(p_X - 0.01)^2 + (p_Y - 0.18)^2 < 0.14^2$ and $0.18 <  p_Y  < 0.32$
$0.1 < \xi < 0.15$	$(p_X + 0.02)^2 + (p_Y - 0.16)^2 < 0.14^2$ and $0.16 <  p_Y  < 0.3$
$0.15 < \xi < 0.2$	$(p_X + 0.04)^2 + (p_Y - 0.16)^2 < 0.12^2$ and $0.16 <  p_Y  < 0.28$
$0.2 < \xi < 0.25$	$(p_X + 0.07)^2 + (p_Y - 0.14)^2 < 0.12^2$ and $0.14 <  p_Y  < 0.26$
$0.25 < \xi < 0.3$	$(p_X + 0.1)^2 + (p_Y - 0.14)^2 < 0.12^2$ and $0.14 <  p_Y  < 0.26$
$0.3 < \xi < 0.35$	$(p_X + 0.11)^2 + (p_Y - 0.12)^2 < 0.12^2$ and $0.12 <  p_Y  < 0.24$
$0.35 < \xi < 0.4$	$(p_X + 0.14)^2 + (p_Y - 0.12)^2 < 0.11^2$ and $0.12 <  p_Y  < 0.23$
$0.4 < \xi < 0.45$	$(p_X + 0.17)^2 + (p_Y - 0.12)^2 < 0.1^2$ and $0.12 <  p_Y  < 0.22$

Table 6.3: Final west RP  $p_X$  and  $p_Y$  cuts

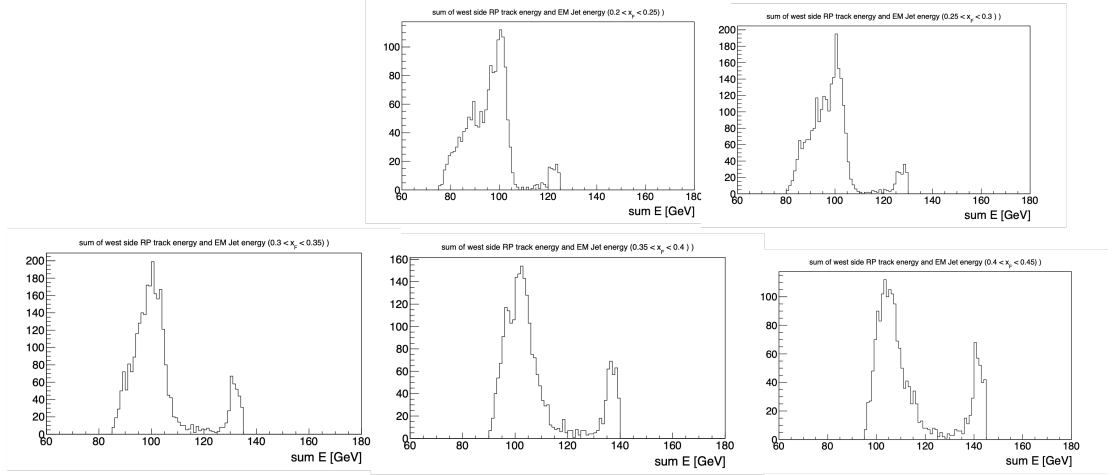


Figure 6.7: Energy sum cuts for 5 different EM-jet  $x_F$  regions

EM-jet $x_F$	Energy sum ( $E_{sum}$ ) cut
0.2 - 0.25	$E_{sum} < 110$ GeV
0.25 - 0.3	$E_{sum} < 110$ GeV
0.3 - 0.35	$E_{sum} < 115$ GeV
0.35 - 0.4	$E_{sum} < 115$ GeV
0.4 - 0.45	$E_{sum} < 120$ GeV

Table 6.4: Energy sum cuts for semi-exclusive process

## 405 Chapter 7

# 406 Background study

### 407 7.1 Zerobias event study

408 The Zerobias events are the highly scaled events with the zerobias trigger. The  
409 details for the events are shown below:

- 410 • Trigger setup name: `production_pp200trans_2015`
- 411 • Data stream: zerobias
- 412 • Production tag: P16id

413 Since there are only a small fraction of events containing good EM-jets at the  
414 FMS, the Zerobias events are only used to estimate the accidental background  
415 for the analysis. To begin with, the NanoDst files are generated from the MuDst  
416 files. For the Zerobias events, there are no requirement on the EM-jets on FMS  
417 and no requirement on RP track. Then, the BBC East veto cuts (detailed in Sec.  
418 (3.3) and East RP track cuts (detailed in Sec. (3.4)) are applied to the Zerobias  
419 events, where both cuts are the same as single diffractive process. About 0.2% of  
420 the events pass the cuts mentioned above. Therefore, about 0.2% of the events  
421 are accidental coincidences and should be the same rate for every process.

422 With the Zerobias events, we also estimate the accidental coincidences (AC)  
423 for the measured single diffractive process. The AC events are coming from the  
424 situation that the FMS EM-jets and the east RP tracks are not correlated. For  
425 example, the FMS EM-jets and the east RP tracks are coming from multiple  
426 collisions, but they are recorded in one event in the data. Equation (7.1) shows  
427 the formula for calculating the fraction for the AC events.  $n_{AC}$  is the number of  
428 the AC events, but it is difficult to count directly.  $n_{mea}$  is the number of event  
429 counts per  $x_F$  bin in the asymmetry calculation for the single diffractive process.  
430  $n_{RG}$  is the number of event counts per  $x_F$  bin in the asymmetry calculation for

431 the RG events, where the description for RG events is in Sec. (5.1).  $\frac{n_{AC}}{n_{RG}}$  can be  
432 considered as the AC events fraction for RG events, which is 0.2%. By counting  
433 the events per  $x_F$  bin for measured single diffractive process and RG events, the  
434 fraction for the AC events is about 1.8% for each  $x_F$  bin. This fraction is small,  
435 so its effect will be assigned to the systematic uncertainty, detailed in Appendix  
436 (B).

$$frac_{bkg} = \frac{n_{AC}}{n_{mea}} = \frac{n_{AC}}{n_{RG}} \times \frac{n_{RG}}{n_{mea}} \quad (7.1)$$

## 437 7.2 Mix event background for energy sum cut 438 study

439 The energy sum cuts constrain the sum of the EM-jet energy and the west  
440 RP track energy. For the accidental coincidence (AC) in the semi-exclusive  
441 process, the energy sum is usually much higher than the beam energy because  
442 the west RP track is coming from the proton from the non-diffractive process,  
443 especially from the elastic scattering process. Therefore, in order to estimate  
444 the contribution to the semi-exclusive events from the AC events, the mix event  
445 background is studied to estimate such contribution.

446 For the mix event background study for energy sum, we use the distribution  
447 for the west RP track energy (momentum) in the zerobias event (7.1), and  
448 the distribution for the EM-jet energy from the inclusive process. The mix  
449 event energy sum background distribution is studied in different EM-jet  $x_F$   
450 regions. The idea for the mix event energy sum background is to calculate all  
451 the possible combinations of the energy sum with west RP track momentum  
452 and EM-jet energy. Equation (7.2) shows the simple idea for the mix event  
453 energy sum calculation (Esum(i+j)). P(i) is the fraction of EM-jet yields in  
454 the inclusive EM-jet energy distribution for [i,i+1] (GeV) within the specific  $x_F$   
455 range. n(j) is the yield in zerobias events west RP momentum distribution for  
456 [j,j+1] (GeV/c). Figure (7.1) shows one example of the mix event energy sum  
457 spectrum. In this example, The left panel of Fig. (7.1) shows the inclusive EM-  
458 jet energy spectrum for  $0.2 < x_F < 0.25$ , which corresponds to  $20 \leq i < 25$ .  
459 The middle panel of Fig. (7.1) shows the zerobias events west RP momentum  
460 distribution, and only west RP momentum between 40 GeV and 100 GeV will  
461 be used for mix event background study, which corresponds to  $40 \leq j < 100$ .  
462 The right panel of Fig. (7.1) show the energy sum distribution using the mix  
463 event background study for EM-jet with  $0.2 < x_F < 0.25$ .

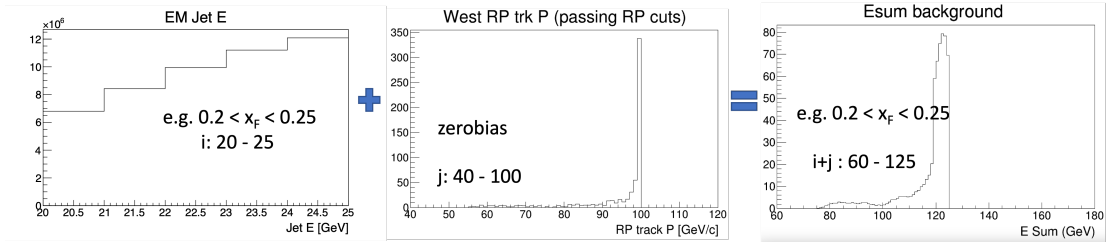


Figure 7.1: Example for mix event energy sum background study for EM-jet with  $0.2 < x_F < 0.25$ .

EM-jet $x_F$	Signal region [GeV]	Background region [GeV]
0.2 - 0.25	Esum < 110 GeV	Esum > 110 GeV
0.25 - 0.3	Esum < 110 GeV	Esum > 110 GeV
0.3 - 0.35	Esum < 115 GeV	Esum > 115 GeV
0.35 - 0.4	Esum < 115 GeV	Esum > 115 GeV
0.4 - 0.45	Esum < 120 GeV	Esum > 120 GeV

Table 7.1: Signal region and background region for energy sum spectrum in data

$$Esum(i + j) = \sum_{i,j} P(i) \times n(j) \quad (7.2)$$

464 Then, we use the shape of the mix event energy sum background to estimate  
465 its contribution to the semi-exclusive events. For the energy sum plots in data,  
466 we define the signal region and the background region based on the energy sum  
467 cut in Sec. (6.3). The signal region and the background region for each EM-jet  
468  $x_F$  region are shown in Tab. (7.1). Then, the shape of the mix event energy  
469 sum background is scaled to the maximum bin value of the background region  
470 in each EM-jet  $x_F$  region. Figure (7.2) shows the mix event background results  
471 for each EM-jet  $x_F$  region. In each plot, the red curve indicates the energy sum  
472 distribution in data, while the black curve indicates the scaled mix event energy  
473 sum background. The fraction of the mix event energy sum background to the  
474 data can be calculated as the ratio of the integrated yields for the scaled mix  
475 event energy sum background within the signal region to the integrated yields  
476 for the data within the signal region. Table (7.2) shows this mix event energy  
477 sum background fraction. Since this fraction is small (less than 3%), we assign  
478 such fraction to the systematic uncertainty as the background term.



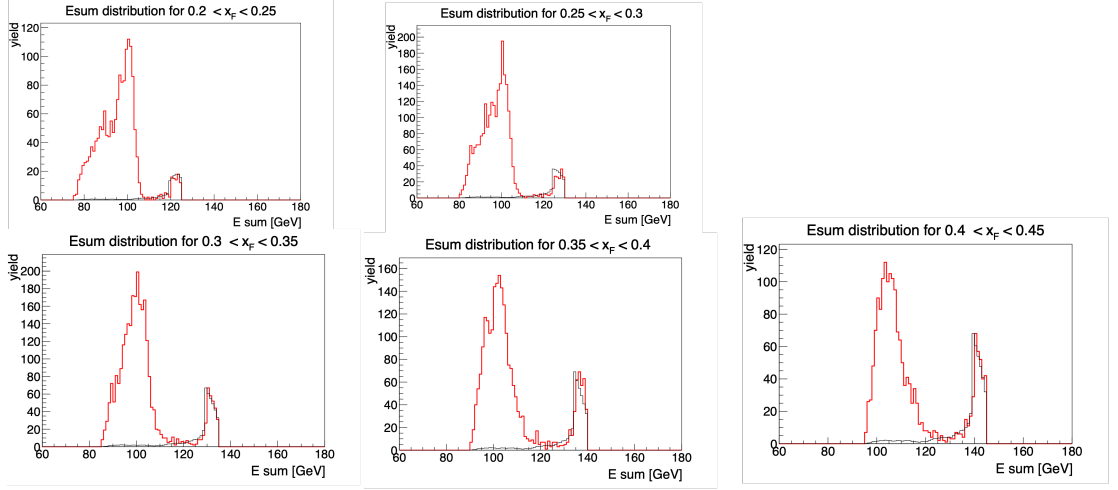


Figure 7.2: Mix event energy sum background study results for each EM-jet  $x_F$  regions. In each plot, the red curve indicates the energy sum distribution in data, while the black curve indicates the scaled mix event energy sum background.

$x_F$	Fraction of background (%)
0.2 - 0.25	1.3
0.25 - 0.3	1.3
0.3 - 0.35	2.1
0.35 - 0.4	2.0
0.4 - 0.45	2.7

Table 7.2: Fraction of the mix event energy sum background for each EM-jet  $x_F$  region

## 479 Chapter 8

# 480 Systematic Uncertainty for 481 $A_N$

482 The systematic uncertainty for single diffractive process includes the cuts on  
483 East BBC veto cuts (details in 8.2), Ring of Fire (details in 8.3) and AC back-  
484 ground (details in 7.1). The systematic uncertainty for rapidity gap events  
485 includes the cuts on East BBC veto cuts (details in 8.2) and Ring of Fire (de-  
486 tails in 8.3). The systematic uncertainty for semi-exclusive process includes the  
487 cuts on West BBC veto cuts (details in 8.2), Ring of Fire (details in 8.3), energy  
488 sum cuts (details in 8.4) and AC background (details in 8.4).

### 489 8.1 Method for systematic uncertainty

490 To study the systematic uncertainty for the BBC veto cuts, Ring of Fire and  
491 the energy sum cuts the Bayesian method is applied [21]. For each term of  
492 systematic uncertainty study, we calculate the  $A_N$  standard deviation among  
493 the variation cuts. However, only the cuts with variations deemed significant  
494 would be included. If a cut with variations produces a maximum value with  
495 statistical uncertainty  $A_N(1) \pm \delta_1$  and a minimum value with statistical uncer-  
496 tainty  $A_N(2) \pm \delta_2$ , only when  $\frac{|A_N(1)-A_N(2)|}{\sqrt{|\delta_1^2-\delta_2^2|}} > 1$  the standard variation will be  
497 used for this systematic uncertainty term, otherwise this systematic uncertainty  
498 term will be assigned 0 (Barlow check) [21]. All the systematic uncertainty for  
499 each  $x_F$  bin will be calculated individually.

Variation	-20	-10	+10	+20
East Large BBC ADC sum cut	60	70	90	100
East Small BBC ADC sum cut	70	80	100	110
West Large BBC ADC sum cut	40	50	70	80
West Small BBC ADC sum cut	60	70	90	100

Table 8.1: List of BBC veto cut values for systematic uncertainty study.

## 500 **8.2 Systematic uncertainty for the BBC veto** 501 **cuts**

502 The BBC veto cuts include East Large BBC ADC sum  $< 80$  and East Small BBC  
503 ADC sum  $< 90$ , for the single diffractive process and the rapidity gap events.  
504 They also include West Large BBC ADC sum  $< 60$  and West Small BBC ADC  
505 sum  $< 80$ , for the semi-exclusive process. We change the cut values for Large  
506 BBC and Small BBC ADC sum to study the systematic uncertainty, as shown  
507 in Tab. (8.1). We calculate the  $A_N$  with its statistical uncertainty for each cut  
508 standard variation with varying the cuts. Then, we use the Barlow check to  
509 determine whether to keep the standard derivation as systematic uncertainty  
510 [21]. Note, the systematic uncertainty for Large BBC and Small BBC ADC  
511 sum cuts are studied separately for each process.

## 512 **8.3 Ring of Fire**

513 The Ring of Fire is a kind of background related to the FMS-sm-bs3 trigger.  
514 This trigger is targeted at the inner region of FMS, which is close to the beam.  
515 It's generally recognized that the beam remnants are accepted by FMS-sm-bs3  
516 trigger. Therefore, the effect of this trigger will be considered as one source of  
517 systematic uncertainty. The systematic uncertainty for the Ring of Fire will  
518 be the  $A_N$  result difference between considering this trigger and excluding this  
519 trigger. In addition, the Barlow check is applied to determine whether to keep  
520 the standard derivation as systematic uncertainty.

## 521 **8.4 Energy sum cut uncertainty**

522 To study the energy sum cut uncertainty, we varied the energy cut per  $x_F$  bin  
523 by  $\pm 10$  GeV and  $\pm 5$  GeV. Table (8.2) shows the exact values for studying the  
524 energy sum cut uncertainty. We calculate the  $A_N$  with its statistical uncertainty  
525 for each cut standard variation with varying these energy sum cuts. Then, we

EM-jet $x_F$	$E_{sum}$ cut (-10 GeV)	$E_{sum}$ cut (-5 GeV)	$E_{sum}$ cut (+5 GeV)	$E_{sum}$ cut (+10 GeV)
0.2 - 0.25	$E_{sum} < 100$ GeV	$E_{sum} < 105$ GeV	$E_{sum} < 115$ GeV	$E_{sum} < 120$ GeV
0.25 - 0.3	$E_{sum} < 100$ GeV	$E_{sum} < 105$ GeV	$E_{sum} < 115$ GeV	$E_{sum} < 120$ GeV
0.3 - 0.35	$E_{sum} < 105$ GeV	$E_{sum} < 110$ GeV	$E_{sum} < 120$ GeV	$E_{sum} < 125$ GeV
0.35 - 0.4	$E_{sum} < 105$ GeV	$E_{sum} < 110$ GeV	$E_{sum} < 120$ GeV	$E_{sum} < 125$ GeV
0.4 - 0.45	$E_{sum} < 110$ GeV	$E_{sum} < 115$ GeV	$E_{sum} < 125$ GeV	$E_{sum} < 130$ GeV

Table 8.2: Energy sum cuts for semi-exclusive process in the energy sum cut uncertainty study

526 use the Barlow check to determine whether to keep the standard derivation as  
527 systematic uncertainty [21].

## 528 8.5 Polarization uncertainty

529 The blue beam and yellow beam polarization are used to calculate the  $A_N$   
530 results. As a habit, the uncertainty of beam polarization uncertainty is listed  
531 independently. The beam polarization measurement results are provided by  
532 the CNI group, which develops, maintains, and operates the RHIC polarimeter  
533 measurement. The beam polarization measurement results are listed in the table  
534 on the webpage [22]. In the webpage, the starting time ( $t_0$ ), the polarization  
535 of the blue (yellow) beam at the beginning of every fill ( $P_0$ ), the decay rate  
536 ( $\frac{dP}{dt}$ ) are provided for each fill. For each event, the beam polarization can be  
537 calculated from the time difference from the beginning of the fill using Equ.  
538 (8.1), where  $t_{event}$  is the time of each event. The beam polarization for each  
539 run can be calculated by Equ. (8.2), where  $t_{run}$  is the time of the center of the  
540 run. The beam polarization for each fill can be calculated using the weighted  
541 average run polarization with Equ. (8.3), where  $L_{run}$  is the luminosity of each  
542 run. However, since  $L_{run}$  is proportional to the number of events in each run,  
543 the number of events in each run will be replacing the luminosity of each run  
544 in the calculation.

$$P_{event} = P_0 + \frac{dP}{dt}(t_{event} - t_0) \quad (8.1)$$

$$P_{run} = P_0 + \frac{dP}{dt}(t_{run} - t_0) \quad (8.2)$$

$$P_{fill} = \frac{\sum_{run} L_{run} P_{run}}{\sum_{run} L_{run}} \quad (8.3)$$

545 The beam polarization uncertainty includes the scale uncertainty, fill-to-fill  
546 uncertainty, and uncertainty from the profile correction procedure [23].

547 The scale uncertainty is related to the polarization measurement methods.  
548 It includes H-jet scale, H-jet background and pC scale. For run 15, the scale

549 uncertainty is 3% [23].

550 The relative uncertainty of the profiles correction for one beam in one fill  
 551 is 2.2%. For a set of M fills, the relative profile correction for the single-spin  
 552 asymmetry measurement is  $\sigma(profile)/P = 2.2\%/\sqrt{M}$  [23]. For the run 15  
 553 FMS dataset, this uncertainty is about 0.3%.

554 The fill-to-fill uncertainty is propagated based on Equ. (8.3) with the uncer-  
 555 tainty of  $P_0$  and  $\frac{dP}{dt}$ . The uncertainty for these two terms ( $\sigma(P_0)$ ) and ( $\sigma(\frac{dP}{dt})$ )  
 556 for either blue beam or yellow beam can be obtained in [22]. This uncertainty  
 557 can be expressed in Equ. (8.4). The third term on the right side of the equation  
 558 is due to the sensitivity of the measurement of the energy scale of the nuclei in  
 559 the pC polarimetry [14], and it's negligible. However, for the term (Equ. (8.5)),  
 560 this correction is overcounting for the measurement using a fraction of the run  
 561 period. Therefore, a correction scale factor  $\sqrt{1 - \frac{M}{N}}$  is applied for the second  
 562 term, which is shown in Equ. (8.6). For this analysis, N=54 and M=142. The  
 563 fill-to-fill uncertainty for single diffractive EM-jet analysis is about 0.3%.

$$\sigma^2(P_{fill}) = \sigma^2(P_0) + \sigma^2\left(\frac{dP}{dt}\right) \cdot \left(\frac{\sum_{run} t_{run} L_{run}}{L_{fill}} - t_0\right)^2 + \left(\frac{\sigma(fill - to - fill)}{P}\right)^2 \cdot P_{fill}^2 \quad (8.4)$$

$$P_{set}^2 = \left(\frac{\sum_{run} t_{run} L_{run}}{L_{fill}}\right) \quad (8.5)$$

$$P_{fill-to-to-fill\ scale}^2 = \left(1 - \frac{N}{M}\right) \cdot P_{set}^2 \quad (8.6)$$

564 Finally, the polarization uncertainty is calculated in the quadrature. For the  
 565 single diffractive EM-jet analysis, it's about 3%.

## 566 8.6 Summary for the systematic uncertainty

567 The final systematic uncertainty for single diffractive process and rapidity gap  
 568 events will be counted bin by bin ( $x_F$  bin), and they are calculated as  $\sqrt{\sum_i \sigma_i^2}$ .

569 Table (8.3) and Table (8.4) show the systematic uncertainty for each and  
 570 final term for the blue beam  $A_N$  and yellow beam  $A_N$  for all photon multiplicity  
 571 EM-jets from single diffractive process, respectively. Table (8.5) and Table (8.6)  
 572 show the systematic uncertainty for each and final term for the blue beam  $A_N$   
 573 and yellow beam  $A_N$  for one or two-photon multiplicity EM-jets from single  
 574 diffractive process, respectively. Table (8.7) and Table (8.8) show the systematic  
 575 uncertainty for each and final term for the blue beam  $A_N$  and yellow beam  $A_N$   
 576 for three or more photon multiplicity EM-jets from single diffractive process,  
 577 respectively.

$x_F$	Small BBC east	Large BBC east	Ring of Fire	Background	Summary
0.2 - 0.25	0.0026	0.0041	0	0.0044	0.0064
0.25 - 0.3	0	0	0.0022	0.0034	0.0041
0.3 - 0.35	0	0.0020	0	0.0032	0.0037
0.35 - 0.4	0.0017	0.0034	0	0.0035	0.0052
0.4 - 0.45	0.0022	0.0052	0.012	0.0041	0.014

Table 8.3: Systematic uncertainty for blue beam  $A_N$  for all photon multiplicity EM-jets from single diffractive process

$x_F$	Small BBC east	Large BBC east	Ring of Fire	Background	Summary
0.2 - 0.25	0.0027	0.0054	0	0.0043	0.0074
0.25 - 0.3	0.0028	0.0025	0	0.0034	0.0051
0.3 - 0.35	0	0.0046	0	0.0031	0.0056
0.35 - 0.4	0.0018	0.0048	0.0051	0.0035	0.0080
0.4 - 0.45	0.0013	0.0022	0	0.0040	0.0048

Table 8.4: Systematic uncertainty for yellow beam  $A_N$  for all photon multiplicity EM-jets from single diffractive process

578 Also, table (8.9) and Table (8.10) show the systematic uncertainty for each  
579 and final term for the blue beam  $A_N$  and yellow beam  $A_N$  for all photon mul-  
580 tiplicity EM-jets from rapidity gap events, respectively. Table (8.11) and Table  
581 (8.12) show the systematic uncertainty for each and final term for the blue beam  
582  $A_N$  and yellow beam  $A_N$  for one or two-photon multiplicity EM-jets from rapid-  
583 ity gap events, respectively. Table (8.13) and Table (8.14) show the systematic  
584 uncertainty for each and final term for the blue beam  $A_N$  and yellow beam  
585  $A_N$  for three or more photon multiplicity EM-jets from rapidity gap events,  
586 respectively.

587 Finally, Table (8.15) and Table (8.16) show the systematic uncertainty for  
588 each and final term for the blue beam  $A_N$  and yellow beam  $A_N$  for one or  
589 two-photon multiplicity EM-jets from semi-exclusive process, respectively.

$x_F$	Small BBC east	Large BBC east	Ring of Fire	Background	Summary
0.2 - 0.25	0.0040	0.0033	0	0.0057	0.0077
0.25 - 0.3	0.0024	0	0.0022	0.0046	0.0056
0.3 - 0.35	0.0018	0.0018	0	0.0044	0.0051
0.35 - 0.4	0.0032	0.0034	0	0.0047	0.0066
0.4 - 0.45	0.0055	0.0072	0.022	0.0052	0.024

Table 8.5: Systematic uncertainty for blue beam  $A_N$  for 1 or 2 photon multiplicity EM-jets from single diffractive process

$x_F$	Small BBC east	Large BBC east	Ring of Fire	Background	Summary
0.2 - 0.25	0.0035	0	0	0.0056	0.0065
0.25 - 0.3	0.0021	0.0035	0	0.0045	0.0061
0.3 - 0.35	0.0025	0.0041	0	0.0043	0.0064
0.35 - 0.4	0	0.0062	0	0.0046	0.0077
0.4 - 0.45	0.0016	0.0036	0.020	0.0052	0.021

Table 8.6: Systematic uncertainty for yellow beam  $A_N$  for 1 or 2 photon multiplicity EM-jets from single diffractive process

$x_F$	Small BBC east	Large BBC east	Ring of Fire	Background	Summary
0.2 - 0.25	0	0.0076	0	0.0068	0.010
0.25 - 0.3	0.0022	0.0028	0.0023	0.0051	0.0066
0.3 - 0.35	0	0	0	0.0046	0.0046
0.35 - 0.4	0	0.0047	0.0076	0.0055	0.010
0.4 - 0.45	0.0035	0.0053	0	0.0066	0.0091

Table 8.7: Systematic uncertainty for blue beam  $A_N$  for 3 or more photon multiplicity EM-jets from single diffractive process

$x_F$	Small BBC east	Large BBC east	Ring of Fire	Background	Summary
0.2 - 0.25	0.0098	0.014	0	0.0067	0.019
0.25 - 0.3	0.0037	0.0033	0	0.0046	0.0071
0.3 - 0.35	0.0030	0.0081	0.0046	0.0045	0.011
0.35 - 0.4	0.0037	0.0047	0.0051	0.0052	0.011
0.4 - 0.45	0	0	0.015	0.0065	0.017

Table 8.8: Systematic uncertainty for yellow beam  $A_N$  for 3 or more photon multiplicity EM-jets from single diffractive process

$x_F$	Small BBC east	Large BBC east	Ring of Fire	Summary
0.1 - 0.2	0	0.0064	0	0.0064
0.2 - 0.25	0.0016	0	0	0.0016
0.25 - 0.3	0.00051	0.00096	0.00042	0.0011
0.3 - 0.35	0.00084	0	0	0.00084
0.35 - 0.4	0.0014	0	0.0033	0.0036
0.4 - 0.45	0.0010	0.0011	0	0.0015

Table 8.9: Systematic uncertainty for blue beam  $A_N$  for all photon multiplicity EM-jets from rapidity gap events

$x_F$	Small BBC east	Large BBC east	Ring of Fire	Summary
0.1 - 0.2	0.0027	0	0	0.0027
0.2 - 0.25	0.00052	0.0019	0	0.0019
0.25 - 0.3	0.00064	0.0012	0	0.0013
0.3 - 0.35	0.00066	0.00047	0	0.00081
0.35 - 0.4	0.00092	0.0013	0.0023	0.0029
0.4 - 0.45	0	0.0012	0	0.0012

Table 8.10: Systematic uncertainty for yellow beam  $A_N$  for all photon multiplicity EM-jets from rapidity gap events

$x_F$	Small BBC east	Large BBC east	Ring of Fire	Summary
0.1 - 0.2	0.0028	0.0061	0	0.0067
0.2 - 0.25	0.0018	0.0019	0	0.0026
0.25 - 0.3	0	0	0.00070	0.00070
0.3 - 0.35	0.00094	0	0.0023	0.0025
0.35 - 0.4	0.0024	0.0017	0	0.0030
0.4 - 0.45	0.00074	0.0019	0	0.0020

Table 8.11: Systematic uncertainty for blue beam  $A_N$  for 1 or 2 photon multiplicity EM-jets from rapidity gap events

$x_F$	Small BBC east	Large BBC east	Ring of Fire	Summary
0.1 - 0.2	0.0027	0	0	0.0027
0.2 - 0.25	0.00081	0.0024	0	0.0018
0.25 - 0.3	0.0015	0.0011	0	0.0019
0.3 - 0.35	0.00086	0.0011	0.0017	0.0022
0.35 - 0.4	0	0.0015	0.0034	0.0037
0.4 - 0.45	0.00069	0	0.0059	0.0060

Table 8.12: Systematic uncertainty for yellow beam  $A_N$  for 1 or 2 photon multiplicity EM-jets from rapidity gap events

$x_F$	Small BBC east	Large BBC east	Ring of Fire	Summary
0.1 - 0.2	0	0.0088	0	0.0088
0.2 - 0.25	0.0015	0	0	0.0015
0.25 - 0.3	0	0	0	0
0.3 - 0.35	0.00082	0	0.0018	0.0020
0.35 - 0.4	0	0	0.0040	0.0040
0.4 - 0.45	0.0028	0.0021	0.0036	0.0050

Table 8.13: Systematic uncertainty for blue beam  $A_N$  for 3 or more photon multiplicity EM-jets from rapidity gap events

$x_F$	Small BBC east	Large BBC east	Ring of Fire	Summary
0.1 - 0.2	0.0045	0	0	0.0045
0.2 - 0.25	0	0.0028	0	0.0028
0.25 - 0.3	0.0014	0.0026	0	0.0029
0.3 - 0.35	0.0014	0	0	0.0014
0.35 - 0.4	0.0017	0.0014	0	0.0022
0.4 - 0.45	0.0017	0.0021	0.0046	0.0053

Table 8.14: Systematic uncertainty for yellow beam  $A_N$  for 3 or more photon multiplicity EM-jets from rapidity gap events



Blue beam $x_F$	Small BBC west	Large BBC west	Ring of Fire	Energy sum	Background	Summary
0.2 - 0.25	0	0.033	0	0.028	0.0033	0.043
0.25 - 0.3	0.0081	0.021	0	0	0.0031	0.023
0.3 - 0.35	0.0058	0	0.010	0.011	0.0027	0.017
0.35 - 0.4	0.0072	0.011	0	0.040	0.0011	0.041
0.4 - 0.45	0.012	0.015	0	0	0.0045	0.019

Table 8.15: Systematic uncertainty for blue beam  $A_N$  for 1 or 2 photon multiplicity EM-jets from semi-exclusive process

Yellow beam $x_F$	Small BBC west	Large BBC west	Ring of Fire	Energy sum	Background	Summary
0.2 - 0.25	0.018	0.014	0	0	0.00059	0.023
0.25 - 0.3	0.012	0	0.0045	0.027	0.00068	0.030
0.3 - 0.35	0	0.015	0	0.0012	0.0011	0.019
0.35 - 0.4	0	0.010	0.017	0	0.0042	0.020
0.4 - 0.45	0	0	0	0.011	0.0032	0.012

Table 8.16: Systematic uncertainty for yellow beam  $A_N$  for 1 or 2 photon multiplicity EM-jets from semi-exclusive process

## 590 Chapter 9

# 591 $A_N$ Analysis Method and 592 Results

### 593 9.1 $A_N$ Extraction

594 The cross-ratio method is used to extract the  $A_N$ , and the corresponding formu-  
595 las are shown in Equ. (9.1) and Equ. (9.2). In both equations, raw  $A_N$  stands  
596 for the raw asymmetry.  $N^{\uparrow(\downarrow)}(\phi)$ ,  $N^{\uparrow(\downarrow)}(\phi + \pi)$  are the yields detected at  $\phi$ ,  
597  $(\phi + \pi)$  for spin up (down) state, where  $\phi$  is the azimuthal angle of the EM-jet  
598 in the lab frame. In this analysis, the full  $2\pi$  azimuthal coverage is split into 16  
599 ranges.  $P$  is the average polarization of the proton beam, where the polariza-  
600 tion for each event is calculated from Equ. (8.1). A cosine fit ( $p_0 \cos(\phi) + p_1$ ) is  
601 applied to the entire data after all the event selection criteria to extract the  $A_N$   
602 from the raw asymmetry in Eq. (9.2), while the constant term  $p_1$  could provide  
603 cross-check for possible unidentified asymmetry, but this analysis does not take  
604 it into account.

$$rawA_N = \frac{\sqrt{N^{\uparrow}(\phi)N^{\downarrow}(\phi + \pi)} - \sqrt{N^{\downarrow}(\phi)N^{\uparrow}(\phi + \pi)}}{\sqrt{N^{\uparrow}(\phi)N^{\downarrow}(\phi + \pi)} + \sqrt{N^{\downarrow}(\phi)N^{\uparrow}(\phi + \pi)}} \quad (9.1)$$

$$\epsilon = PA_N \cos(\phi) \quad (9.2)$$

605 This method takes advantage of detector azimuthal symmetry and cancels  
606 effects due to the non-uniform detector efficiency and the time-dependent lumi-  
607 nosity.

608 Figure 9.1 shows one example for the raw asymmetry extraction with the  
609 cosine fit applied. Finally, the quality of the cross-ratio fit for all these processes  
610 and the cases of photon multiplicity are mentioned in Appendix C.

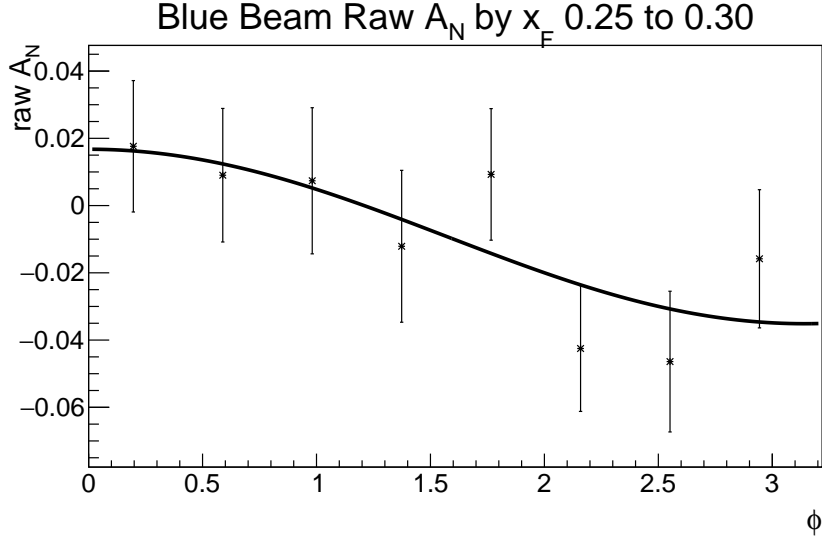


Figure 9.1: Example of the raw asymmetry (raw  $A_N$ ) extraction with the cosine fit. This is the fit for calculating the raw asymmetry for single diffractive EM-jet  $A_N$  with all photon multiplicity at the EM-jet  $0.25 < x_F < 0.3$ .

## 9.2 Single diffractive EM-jet $A_N$

Three cases of EM-jet are studied for  $A_N$  of the single diffractive process: the EM-jet with all photon multiplicity, with only one or two-photon multiplicity, and with three or more photon multiplicity. Figure (9.2) shows the results for the single diffractive EM-jet  $A_N$  as a function of  $x_F$  for the three cases of photon multiplicity mentioned above. Among the three panels in the figure, the blue points are for the blue beam  $A_N$ , represented as  $x_F > 0$ , while the red points are for the yellow beam  $A_N$ , represented as  $x_F < 0$ . The top panel is the results for all photon multiplicity. The statistical uncertainty is shown in bar, while the systematic uncertainty is shown in shaded box. The  $2.7 \sigma$  non-zero significance is observed for the blue beam  $A_N$ . The blue beam  $A_N$  for the EM-jets with one or two photon multiplicity case shows about  $2.5 \sigma$  non-zero significance, showing in the middle panel. However, the blue beam  $A_N$  for the EM-jets with three or more photon multiplicity cases is consistent with zero. The EM-jet  $A_N$  for one or two-photon multiplicity case is larger than that for all photon multiplicity case and for three or more-photon multiplicity case, which is consistent with the results shown in the inclusive processes [24].

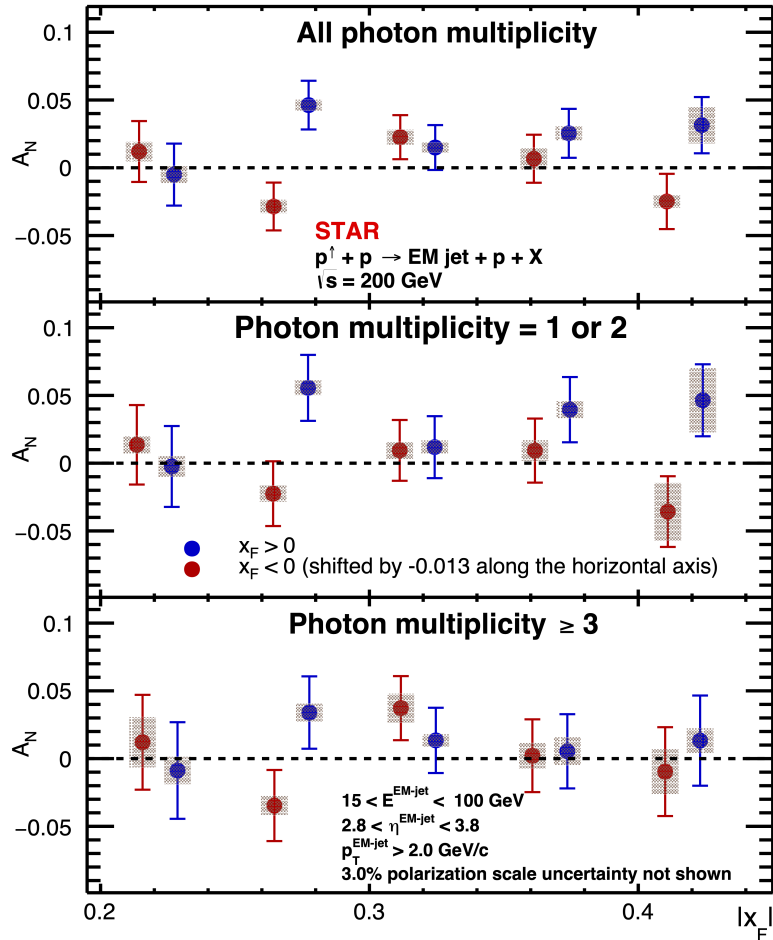


Figure 9.2:  $A_N$  for single diffractive events as a function of  $x_F$  for three different photon multiplicity cases: all photon multiplicity (top), one or two-photon multiplicity (middle), and three or more photon multiplicity (bottom). The  $A_N$  for  $x_F < 0$  (red points) shifts -0.013 along the x-axis.

### 628 **9.3 Rapidity gap events EM-jet $A_N$**

629 For the  $A_N$  of the rapidity gap events, the same three cases of the EM-jet are  
630 explored: the EM-jet with all photon multiplicity, with only one or two-photon  
631 multiplicity, and with three or more photon multiplicity. Figure (9.3) shows the  
632 results for the EM-jet  $A_N$  of the rapidity gap events as a function of  $x_F$  for  
633 the three cases of photon multiplicity mentioned above. The  $A_N$  of all photon  
634 multiplicity and one or two-photon multiplicity cases shows the non-zero value  
635 but with a similar scale as for the  $A_N$  of the inclusive process with the same  
636 two cases of photon multiplicity [24]. The  $A_N$  of the three or more photon  
637 multiplicity EM-jets are shown to be consistent with zero. In addition, the  
638 yellow beam  $A_N$  is also consistent with zero, regardless of photon multiplicity.

639 Furthermore, to better visualize the  $A_N$  contributions of the single diffractive  
640 process and the rapidity gap events to the inclusive process, a direct comparison  
641 plot among the  $A_N$  for inclusive process, diffractive process, and rapidity gap  
642 events for one or two-photon multiplicity, and three or more-photon multiplic-  
643 ity are shown in Fig. (9.4). The  $A_N$  for the single diffractive process and the  
644 rapidity gap events are consistent with that for inclusive process within uncer-  
645 tainty coverage for most of the  $x_F$  regions for both multiplicity cases. The  $A_N$   
646 for the three processes for EM-jets with three or more-photon multiplicity are  
647 all consistent with each other. These direct comparison results indicate that  
648 the single diffractive process can not provide evidence that it contributes to the  
649 large  $A_N$  in the inclusive process.

### 650 **9.4 Semi-exclusive EM-jet $A_N$**

651 For the semi-exclusive process, only the case of EM-jet with 1 or 2 photon is  
652 explored to extract the  $A_N$ , because the majority of the events are with 1 or  
653 2 photon multiplicity EM-jet. Figure (9.5) shows the semi-exclusive EM-jet  
654  $A_N$  as a function of EM-jet  $x_F$ . Constant fit is applied to check the n-sigma  
655 significance for non-zero  $A_N$  value among these  $x_F$  regions. The blue beam  
656  $A_N$  is  $3.1\sigma$  to be non-zero, while the yellow beam  $A_N$  is  $1.4\sigma$  to be non-zero.  
657 However, the semi-exclusive EM-jet  $A_N$  is negative, which is different from  $A_N$   
658 in the inclusive process. Further theories are needed to understand such different  
659 sign.

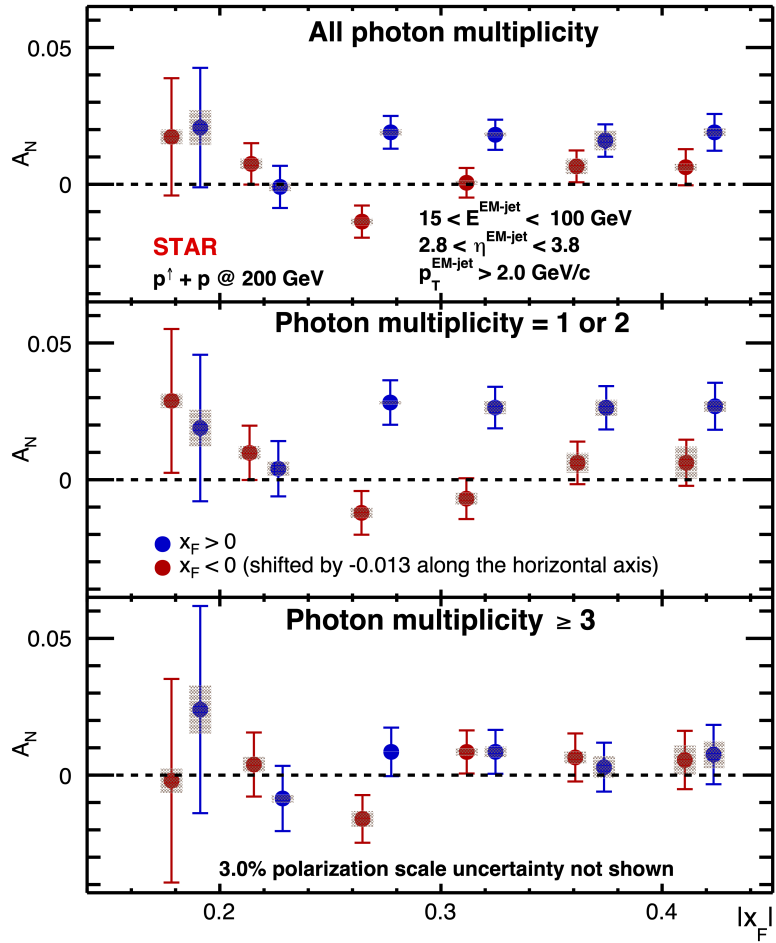


Figure 9.3:  $A_N$  for rapidity gap events as a function of  $x_F$  for three different photon multiplicity cases: all photon multiplicity (top), one or two-photon multiplicity (middle), and three or more photon multiplicity (bottom). The  $A_N$  for  $x_F < 0$  (red points) shifts -0.013 along the x-axis.

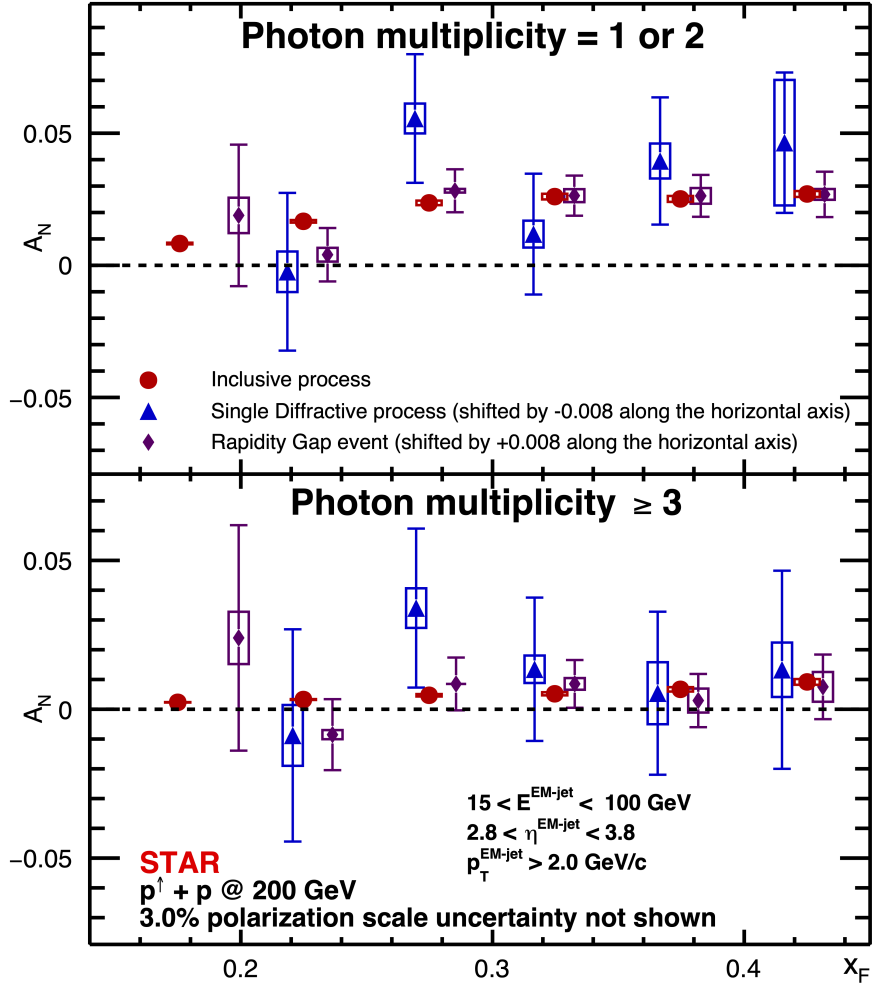


Figure 9.4:  $A_N$  for inclusive process (red), single diffractive process (blue), and the rapidity gap events (purple) as a function of  $x_F$  for one or two-photon multiplicity case (top panel) and three or more-photon multiplicity (bottom panel). The  $A_N$  for single diffractive process shifts -0.008 along the x-axis, and the  $A_N$  for rapidity gap events shifts +0.008 along the x-axis

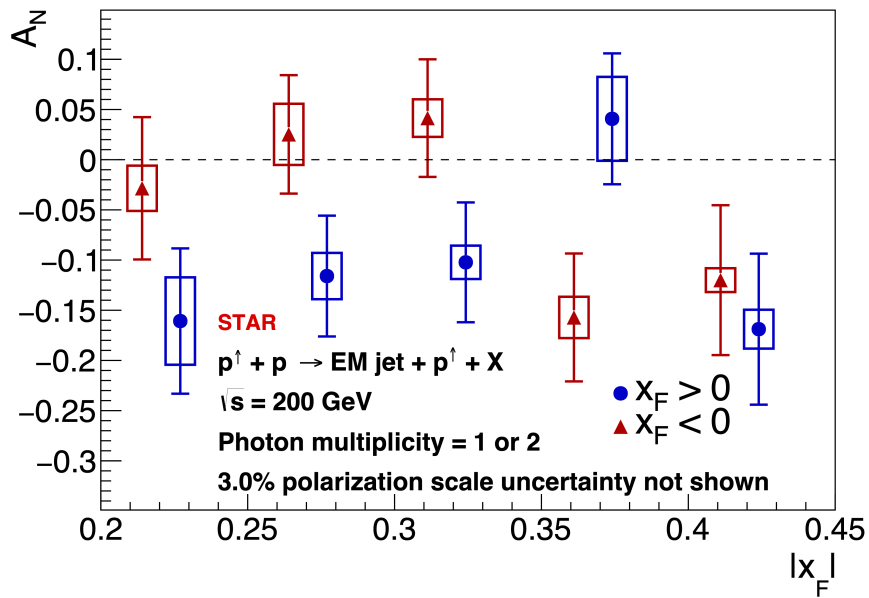


Figure 9.5:  $A_N$  for the semi-exclusive process with 1 or 2 photon multiplicity EM-jets as a function of EM-jet  $x_F$ . The blue points are for  $x_F > 0$ , while the red points are for  $x_F < 0$ .



## Chapter 10

# Cross section fraction study

The cross section fraction is the fraction of the cross section in the single diffractive process to the cross section in the inclusive process at forward region. This study can provide evidence to develop theories to understand the underlying mechanism for the  $A_N$  in the diffractive process.

The cross section for the single diffractive process ( $\sigma_{SD}$ ) can be calculated using Equ. (10.1). The cross section for the inclusive process ( $\sigma_{inc}$ ) can be calculated using Equ. (10.2).  $N_{SD}$  and  $N_{inc}$  denote as the yields of single diffractive events and inclusive events, respectively.  $\varepsilon_{RP}$  and  $\varepsilon_{BBC}$  are the Roman Pot efficiency and BBC efficiency, respectively. Purity indicate the fraction of the real single diffractive process in the single diffractive process.  $\varepsilon_{FMS}$  denotes as FMS efficiency,  $\varepsilon_{trigger}$  denotes as trigger efficiency,  $\mathcal{L}$  denotes as integrated luminosity. However, it is difficult to calculate the FMS efficiency and the trigger efficiency. Therefore, we do not calculate the absolute cross section for either process. However, if we assume the FMS efficiency, the trigger efficiency and the integrated luminosity are the same between two processes, all these terms can cancel out between each other when we calculate their ratio. In that case, the cross section fraction can be calculated using Equ. (10.3).

$$\sigma_{SD} = \frac{N_{SD} \times purity}{\mathcal{L} \times \varepsilon_{RP} \times \varepsilon_{BBC} \times \varepsilon_{FMS} \times \varepsilon_{trigger}} \quad (10.1)$$

$$\sigma_{inc} = \frac{N_{inc}}{\mathcal{L} \times \varepsilon_{FMS} \times \varepsilon_{trigger}} \quad (10.2)$$

$$\frac{\sigma_{SD}}{\sigma_{inc}} = \frac{N_{SD} \times purity}{N_{inc} \times \varepsilon_{RP} \times \varepsilon_{BBC}} \quad (10.3)$$

Purity can be calculated using the zerobias event background estimation (detail in Sec. (7.1)). The fraction of the accidental coincidence is  $1.8\% \pm 0.1\%$ ,

681 so the purity is  $98.2\% \pm 0.1\%$ .

682 The RP efficiency can be estimated using the single diffractive process sim-  
683 ulation using the Pythia simulation and RP simulation (pp2pp). It can be  
684 calculated by the fraction of the events with good east RP track after the RP  
685 simulation in the detector level to the events with proton on east side in the  
686 Pythia simulation in the particle level. Both the good east RP track in the RP  
687 simulation and the proton track in the particle level simulation are required to  
688 be within  $0 < \xi < 0.15$  region. The RP efficiency is about 11.4%.

689 The BBC efficiency be estimated using the single diffractive process simu-  
690 lation using the Pythia simulation and STAR simulation (Geant3) with BBC  
691 simulation option. This efficiency can be calculated by the fraction of the events  
692 passing the BBC east veto (detail in Sec. (3.3)) to all the events with east proton  
693 intact. The BBC efficiency is about 99.9%.

694 The systematic uncertainty for the RP efficiency is 6.5%, based on the STAR  
695 central exclusive analysis [25]. The systematic uncertainty for the BBC efficiency  
696 is 10%, based on STAR single diffractive study [26].

697 The overall cross section fraction is  $0.586\% \pm 0.070\%$ . The differential cross  
698 section is studied as a function of EM-jet  $x_F$  region, shown in Fig. (10.1). The  
699 single diffractive process cross section is very small compared to the inclusive  
700 process cross section, which shows that it can not have significant contribution  
701 to the large  $A_N$  in inclusive process.

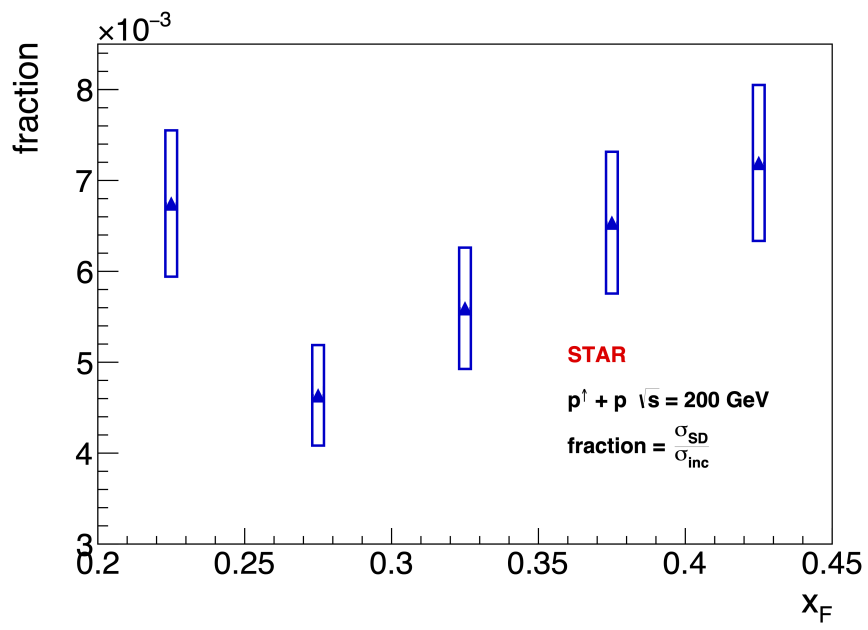


Figure 10.1: Cross section fraction of the single diffractive process ( $\sigma_{SD}$ ) to the inclusive process ( $\sigma_{inc}$ ) as a function of  $x_F$ .

## 702 Chapter 11

## 703 Conclusion

704 The transverse single-spin asymmetry as a function of EM-jet  $x_F$  from single  
705 diffractive process is explored. The all photon multiplicity and one or two-  
706 photon multiplicity EM-jet  $A_N$  for  $x_F > 0$  from the single diffractive process  
707 show the non-zero values with more than  $2\text{-}\sigma$  significance. The  $A_N$  for  $x_F < 0$   
708 from the single diffractive process and rapidity gap events are shown to be  
709 consistent with zero. Furthermore, the  $A_N$  for inclusive process, the single  
710 diffractive process, and the rapidity gap events are consistent with each other  
711 within uncertainty. In addition, the cross section fraction study provide evidence  
712 that the single diffractive process cross section is very small compared to the  
713 inclusive process cross section. Therefore, no strong evidence exists that these  
714 process with the unpolarized proton intact will contribute to the large  $A_N$  in  
715 the inclusive process.

716 The transverse single-spin asymmetry for semi-exclusive process with polar-  
717 ized proton intact is negative with more than  $3\sigma$  significance to be non-zero,  
718 which also can not have great contribution to the large  $A_N$  in the inclusive  
719 process. Such a different sign on the  $A_N$  requires further theories to explain.

720 **Appendix A**

721 **Run list**

Table A.1: Run list

16066033	16066035	16066046	16066047	16066049	16066050	16066051
16066052	16066053	16066054	16066055	16066059	16066060	16067001
16067003	16067004	16067005	16067006	16067013	16067014	16067015
16067016	16067017	16067019	16067020	16067021	16067022	16068022
16068023	16068024	16068025	16068028	16068029	16068030	16068032
16068034	16068035	16068036	16068037	16068038	16068039	16068040
16068042	16068055	16068056	16068057	16068058	16069001	16069002
16069003	16069004	16069005	16069006	16069007	16069008	16069009
16069010	16069011	16069012	16069016	16069053	16069054	16069055
16069060	16069062	16069063	16069064	16069065	16069066	16069067
16070003	16070004	16070005	16070006	16070008	16070009	16070010
16070012	16070013	16070014	16070015	16070039	16071001	16071002
16071003	16071006	16071007	16071010	16071016	16071018	16071021
16071022	16071023	16071024	16071025	16071026	16071027	16071043
16071044	16071045	16071046	16071050	16071051	16071052	16071053
16071054	16071055	16071056	16071058	16071059	16071060	16071061
16071062	16071076	16071077	16071078	16071079	16072001	16072002
16072003	16072006	16072007	16072008	16072009	16072010	16072012
16072013	16072014	16072021	16072022	16072023	16072024	16072025

Table A.1: Run list (Continued)

16072026	16072033	16072034	16072035	16072036	16072038	16072039
16072040	16072041	16072042	16072043	16072046	16072047	16072057
16072058	16072059	16072060	16072061	16072062	16073001	16073017
16073018	16073019	16073020	16073021	16073030	16073031	16073032
16073033	16073034	16073035	16073037	16073038	16073039	16073040
16077021	16077027	16077028	16077029	16077030	16077031	16077032
16077033	16077034	16077037	16077038	16077039	16077040	16077041
16077043	16077044	16077045	16077046	16077047	16077054	16077055
16078001	16078002	16078003	16078004	16078005	16078006	16078007
16078008	16078009	16078011	16078012	16078013	16078014	16078028
16078029	16078030	16078031	16078032	16078033	16078034	16078035
16078036	16078037	16078038	16078039	16078040	16078041	16078042
16078055	16078056	16079001	16079010	16079011	16079013	16079014
16079015	16079016	16079017	16079018	16079019	16079020	16079021
16079022	16079023	16079024	16079027	16079028	16079029	16079030
16079031	16079032	16079033	16079034	16079035	16079036	16079045
16079046	16079047	16079054	16079057	16079058	16079059	16079060
16079061	16079062	16079063	16080002	16080003	16080004	16080005
16080006	16080007	16080012	16080013	16080014	16080015	16080020
16080021	16080022	16080023	16080024	16080025	16080026	16080027
16080028	16080029	16080030	16080031	16080032	16080033	16080043
16080044	16080045	16080046	16080047	16080048	16080049	16080050
16080051	16080052	16080053	16080054	16080055	16081001	16081002
16081003	16081004	16081012	16081013	16081015	16081016	16081017
16081018	16081019	16081020	16081021	16081022	16081024	16081025
16081036	16081037	16081048	16081049	16081050	16081052	16081053
16081054	16081055	16081056	16081057	16081058	16081059	16081060
16081061	16082001	16082002	16082011	16082012	16082013	16082017
16082018	16082019	16082022	16082023	16082025	16082027	16082028

Continued on next page

Table A.1: Run list (Continued)

16082029	16082039	16082040	16082041	16082042	16082043	16082045
16082046	16082047	16082048	16082049	16082050	16082051	16082052
16082053	16082054	16082055	16082056	16082057	16083004	16083005
16083006	16083007	16083008	16083009	16083010	16083011	16083012
16083013	16083014	16083015	16083016	16083017	16083018	16083019
16083041	16083042	16083043	16083044	16083045	16083046	16083048
16083049	16083050	16083052	16083053	16083055	16083056	16083057
16083058	16083059	16083060	16084004	16084006	16084007	16084008
16084009	16084011	16084012	16084013	16084014	16084015	16085005
16085006	16085007	16085008	16085009	16085011	16085012	16085013
16085014	16085023	16085024	16085025	16085026	16085027	16085028
16085029	16085030	16085031	16085032	16085033	16085035	16085036
16085037	16085051	16085052	16085054	16085055	16085056	16085057
16085058	16085061	16085062	16085065	16085067	16085069	16085071
16085072	16085073	16085074	16086001	16086002	16086003	16086004
16086005	16086006	16086007	16086008	16086024	16086025	16086026
16086027	16086028	16086030	16086031	16086032	16086033	16086034
16086035	16086036	16086037	16086038	16086039	16086040	16086041
16086042	16086050	16086051	16086052	16086053	16086054	16087001
16087002	16087003	16087004	16087005	16087006	16087007	16087008
16087009	16087010	16087011	16087019	16087020	16087021	16087022
16087023	16087024	16087025	16087026	16087027	16087028	16087029
16087030	16087031	16087032	16087033	16087041	16087042	16087043
16087044	16087045	16087046	16087047	16087048	16087049	16087050
16087051	16087052	16087053	16087054	16087055	16088001	16088013
16088016	16088017	16088018	16088019	16088020	16088021	16088022
16088023	16088025	16088026	16088027	16088028	16088029	16088030
16088031	16088040	16088041	16088042	16088043	16088044	16088045
16088046	16088047	16088048	16088049	16088050	16089001	16089002

Continued on next page

Table A.1: Run list (Continued)

16089003	16089004	16089005	16089015	16089016	16089017	16089018
16089019	16089020	16089024	16089026	16089027	16089028	16089029
16089030	16089031	16089041	16089042	16089043	16089044	16089045
16089046	16089047	16089048	16089049	16089050	16089051	16089052
16089053	16089054	16090001	16090002	16090003	16090004	16090005
16090015	16090016	16090017	16090018	16090019	16090020	16090021
16090022	16090023	16090024	16090025	16090026	16090027	16090028
16090029	16090030	16090038	16090039	16090041	16090042	16090044
16090045	16090046	16090047	16090048	16090049	16090050	16090051
16090052	16090053	16091003	16091004	16091005	16091006	16091007
16091008	16091009	16091010	16091011	16091012	16091013	16091014
16091039	16091040	16091042	16091057	16091061	16091062	16091063
16092001	16092002	16092003	16092014	16092015	16092016	16092017
16092018	16092019	16092020	16092021	16092022	16092023	16092031
16092033	16092034	16092035	16092036	16092037	16092040	16092042
16092044	16092048	16092049	16092050	16092051	16092052	16092053
16092054	16092055	16092063	16092064	16092065	16092066	16092067
16092068	16092069	16092070	16092071	16093001	16093002	16093003
16093004	16093010	16093011	16093012	16093013	16093014	16093015
16093016	16093017	16093018				

725



## 726 Appendix B

# 727 Derivation for the AC 728 events effect to the 729 uncertainty

730 The effect for the uncertainty in  $A_N$  calculation regarding the AC events is  
731 derived as follows. First of all, the corrected  $A_N$  is shown in Equ. (B.1).  
732  $A_N(sig)$  is the corrected  $A_N$ , while  $A_N(mea)$  is the measured  $A_N$  which contains  
733 the effect of AC events.  $frac(sig)$  is the signal fraction, while  $frac(bkg)$  is the  
734 AC background fraction, which is about 1.8% (detailed in Sec. (7.1)). The error  
735 propagation for Equ. (B.1) is expressed in Equ. (B.2). Since the AC background  
736 fraction and its uncertainty are very small, the second and the third term are  
737 neglectable. Therefore, only the first term related to the statistical uncertainty  
738 of the measured asymmetry will be kept. The difference in the uncertainty  
739 between with and without the AC event correction will be assigned as systematic  
740 uncertainty.

$$A_N(sig) = \frac{A_N(mea) - frac(bkg) * A_N(bkg)}{frac(sig)} = \frac{A_N(mea) - frac(bkg) * A_N(bkg)}{1 - frac(bkg)} \quad (B.1)$$

$$\begin{aligned}
\sigma^2 &= \left(\frac{\partial A_N(\text{sig})}{\partial A_N(\text{mea})}\right)^2 \sigma A_N^2(\text{mea}) + \left(\frac{\partial A_N(\text{sig})}{\partial \text{frac}(\text{bkg})}\right)^2 \sigma \text{frac}^2(\text{bkg}) + \left(\frac{\partial A_N(\text{sig})}{\partial A_N(\text{bkg})}\right)^2 \sigma A_N^2(\text{bkg}) \\
&= \left(\frac{1}{1 - \text{frac}(\text{bkg})}\right)^2 \sigma A_N^2(\text{mea}) + \left(\frac{A_N(\text{sig})}{1 - \text{frac}(\text{bkg})}\right)^2 \sigma \text{frac}^2(\text{bkg}) + \left(\frac{\text{frac}(\text{bkg})}{1 - \text{frac}(\text{bkg})}\right)^2 \sigma A_N^2(\text{bkg}) \\
&= \left(\frac{1}{\text{frac}(\text{sig})}\right)^2 \sigma A_N^2(\text{mea}) + \left(\frac{A_N(\text{sig})}{\text{frac}(\text{sig})}\right)^2 \sigma \text{frac}^2(\text{bkg}) + \left(\frac{\text{frac}(\text{bkg})}{\text{frac}(\text{sig})}\right)^2 \sigma A_N^2(\text{bkg}) \\
&\approx \left(\frac{1}{\text{frac}(\text{sig})}\right)^2 \sigma A_N^2(\text{mea})
\end{aligned}
\tag{B.2}$$

## 741 Appendix C

# 742 Cross-ratio fit quality 743 results

744 Figure C.1 shows the  $\chi^2$  for the fit on extracting the  $A_N$  for all the three  
745 processes mentioned in this note. Figure C.2 shows the distribution of the  
746 constant term from the fit divided by its uncertainty. A Gaussian fit is applied  
747 to check whether the constant term is consistent with zero. The mean of the  
748 Gaussian fit is  $-0.15 \pm 0.16$  and the width is  $1.1 \pm 0.15$ , which show that the  
749 constant term is consistent with zero within uncertainty.

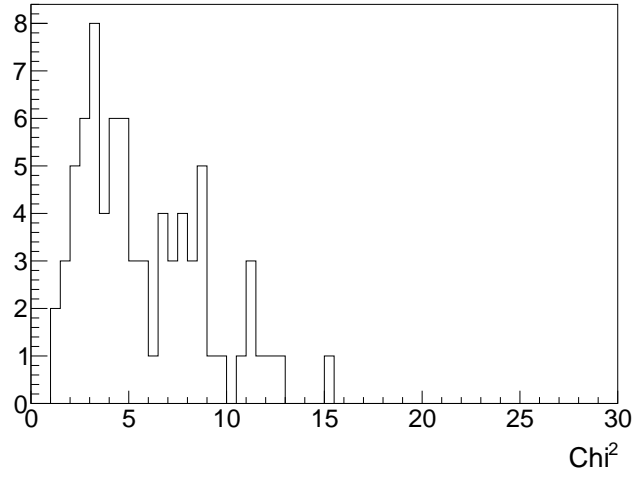


Figure C.1:  $\chi^2$  for the fit for all the data points for all three processes.

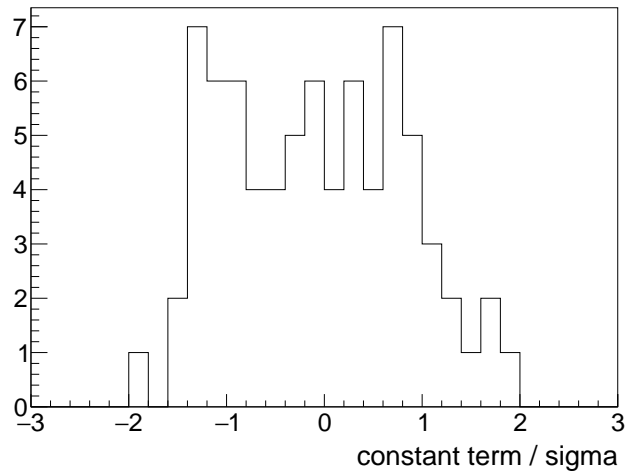


Figure C.2: Distribution of the constant term from the fit divided by its uncertainty

# 750 Bibliography

- 751 [1] D.L. Adams *et al.*, Phys. Lett. B 261, 201(1991)
- 752 [2] B.I. Abelev *et al.* (STAR Collaboration), Phys. Rev. Lett. 101,  
753 222001(2008)
- 754 [3] A. Adare *et al.* Phys. Rev. D 90, 012006 (2014)
- 755 [4] E.C. Aschenauer *et al.*, arXiv:1602.03922
- 756 [5] J. Adam *et al.* (STAR Collaboration), Phys. Rev. D 103, 092009 (2021)
- 757 [6] G. L. Kane, J. Pumplin, and W. Repko. Phys. Rev. Lett. 41, 1689 (1978)
- 758 [7] D. Sivers, Phys. Rev. D 41, 83 (1990)
- 759 [8] J. Collins, Nucl Phys B 396 (1993) 161
- 760 [9] J.W. Qiu and G. Sterman, Phys. Rev. Lett. 67 2264 (1991)
- 761 [10] V. Khachatryan *et al.* (CMS Collaboration)
- 762 [11] M.M. Mondal (STAR Collaboration) PoS (DIS2014) 216 Phys. Rev. D 92,  
763 012003 (2015)
- 764 [12] C. Kim, <https://drupal.star.bnl.gov/STAR/starnotes/private/psn0735>
- 765 [13] M.Cacciari, G. P. Salam, and G. Soyez, Eur. Phys. J. C (2012) 72: 1896
- 766 [14] Z. Zhu, [https://drupal.star.bnl.gov/STAR/system/files/AnalysisNote\\_0601\\_0.pdf](https://drupal.star.bnl.gov/STAR/system/files/AnalysisNote_0601_0.pdf)
- 767 [15] J. Adam *et al.* (STAR Collaboration), Results on Total and Elastic Cross  
768 Sections in Proton–Proton Collisions at  $\sqrt{s} = 200$  GeV, Phys. Lett. B 808  
769 (2020) 135663
- 770 [16] Particle Data Group, The review of particle physics, Prog. Theor. Exp.  
771 Phys. (2020) 083C01.
- 772 [17] B. B. Abelev *et al.* (ALICE Collaboration), Phys. Rev. D 91, 112012 (2015)

- 773 [18] T. Sjostrand, S. Mrenna, and P. Z. Skands, JHEP 05, 026 (2006)
- 774 [19] P. Skands, arXiv:1005.3457
- 775 [20] Peter Z. Skands Phys. Rev. D 82, 074018
- 776 [21] R. Barlow, Systematic Errors: facts and fictions, arXiv:hep-ex/0207026
- 777 [22] Run 15 polarization , [https://wiki.bnl.gov/rhicspin/Run\\_15\\_polarization](https://wiki.bnl.gov/rhicspin/Run_15_polarization)
- 778 [23] W. B. Schmidke, RHIC polarization for Runs 9-17 , Technical Report BNL-  
779 209057-2018- TECH, Brookhaven National Laboratory (2018)
- 780 [24] X. Liang (STAR Collaboration) 10.5281/zenodo.7236716
- 781 [25] The STAR collaboration., Adam, J., Adamczyk, L. et al. Measurement of  
782 the central exclusive production of charged particle pairs in proton-proton  
783 collisions at  $\sqrt{s} = 200$  GeV with the STAR detector at RHIC. J. High  
784 Energ. Phys. 2020, 178 (2020). [https://doi.org/10.1007/JHEP07\(2020\)178](https://doi.org/10.1007/JHEP07(2020)178)
- 785 [26] STAR analysis note, Measurement of charged-particle production in single  
786 diffractive proton-proton collisions at  $\sqrt{s} = 200$  GeV with the STAR de-  
787 tector at RHIC , <https://drupal.star.bnl.gov/STAR/system/files/nota.pdf>